Very Low-grade Metamorphic Evolution of Pelitic Rocks under High-pressure/Low-temperature Conditions, NW New Caledonia (SW Pacific)

S. POTEL*, R. FERREIRO MÄHLMANN†, W. B. STERN, J. MULLIS AND M. FREY‡

MINERALOGISCH–PETROGRAPHISCHES INSTITUT DER UNIVERSITÄT BASEL, BERNOULLISTRASSE 30, CH-4056 BASEL, SWITZERLAND

The P–T gradient in a Late Eocene low-T high-P metamorphic belt in northern New Caledonia increases from SW to NE. Metapelites in the pumpellyite–prehnite and blueschist zones contain lawsonite, Mg-carpholite, Fe-stilpnomelane and Fe-glaucophane. Thermodynamic calculations indicate a progression of metamorphic conditions from less than 0·3 GPa and 250°C in a kaolinite-bearing rock in the SW, up to 1·5 GPa and 410°C in a lawsonite–glaucophane-bearing sample in the NE of the Diahot terrane. Through a multi-method investigation of phyllosilicates, organic matter and fluid inclusions, we demonstrate that the evolution of organic matter and illite crystallinity depends strongly on the evolution of the P–T path with time. In addition, we show that the illite–muscovite b cell dimension provides a robust estimate of maximum pressure reached in low-temperature domains with polyphase metamorphic histories, despite subsequent high-temperature–low-pressure events. Fluid inclusion study reveals an isothermal decompression in the Diahot terrane.

INTRODUCTION

Since the first study by Brothers (1970), New Caledonia has been well known for its Eocene high-pressure (HP) metamorphic belt located in the northern part of the island. In the central and NE of the metamorphic belt, the Koumac and Diahot terranes (Cluzel *et al.*, 1994) (Fig. 1), which are composed of Cretaceous to Eocene metasediments and metavolcanics, are characterized by diagenetic to blueschist-facies assemblages. These terranes have been the subject of numerous petrological studies (Brothers, 1970; Brothers & Black, 1973; Black & Brothers, 1977; Diessel *et al.*, 1978; Brothers & Yokohama, 1982; Ghent *et al.*, 1987; Black *et al.*, 1993; Cluzel *et al.*, 1994; Clarke *et al.*, 1997; Carson *et al.*, 2000; Fitzherbert *et al.*, 2003), which focused on the lawsonite–albite-bearing schists in the SW of the Diahot terrane and omphacite–garnet schists in the Pouébo terrane. The very low-grade metamorphism has received limited attention, focusing on the determination of mineral assemblage stability fields and the mapping of mineral isograds (Black, 1975, 1977; Black & Brothers, 1977), and the evolution of organic material (Diessel *et al.*, 1978).

In the study of very low- and low-grade metamorphic rocks, maturation of organic matter and reaction progress, and development of clay minerals, are useful tools to describe the thermal evolution during metamorphism. Vitrinite reflectance (VR) is an important maturity parameter that can be used to determine the transition

*Corresponding author. Present address: Geologisch–Palaeontologisches Institut, Senckenberganlage 32–34, D-60054 Frankfurt am Main, Germany. E-mail: s.potel@em.uni-frankfurt.de
†Present address: Fachbereich Material- und Geowissenschaften, Technische Petrologie, Schnittspahnstrasse 9, D-64287 Darmstadt, Germany.
‡Martin Frey died in an accident in the Swiss Alps on September 10, 2000. Our work is dedicated to him, an excellent researcher and a friendly colleague.
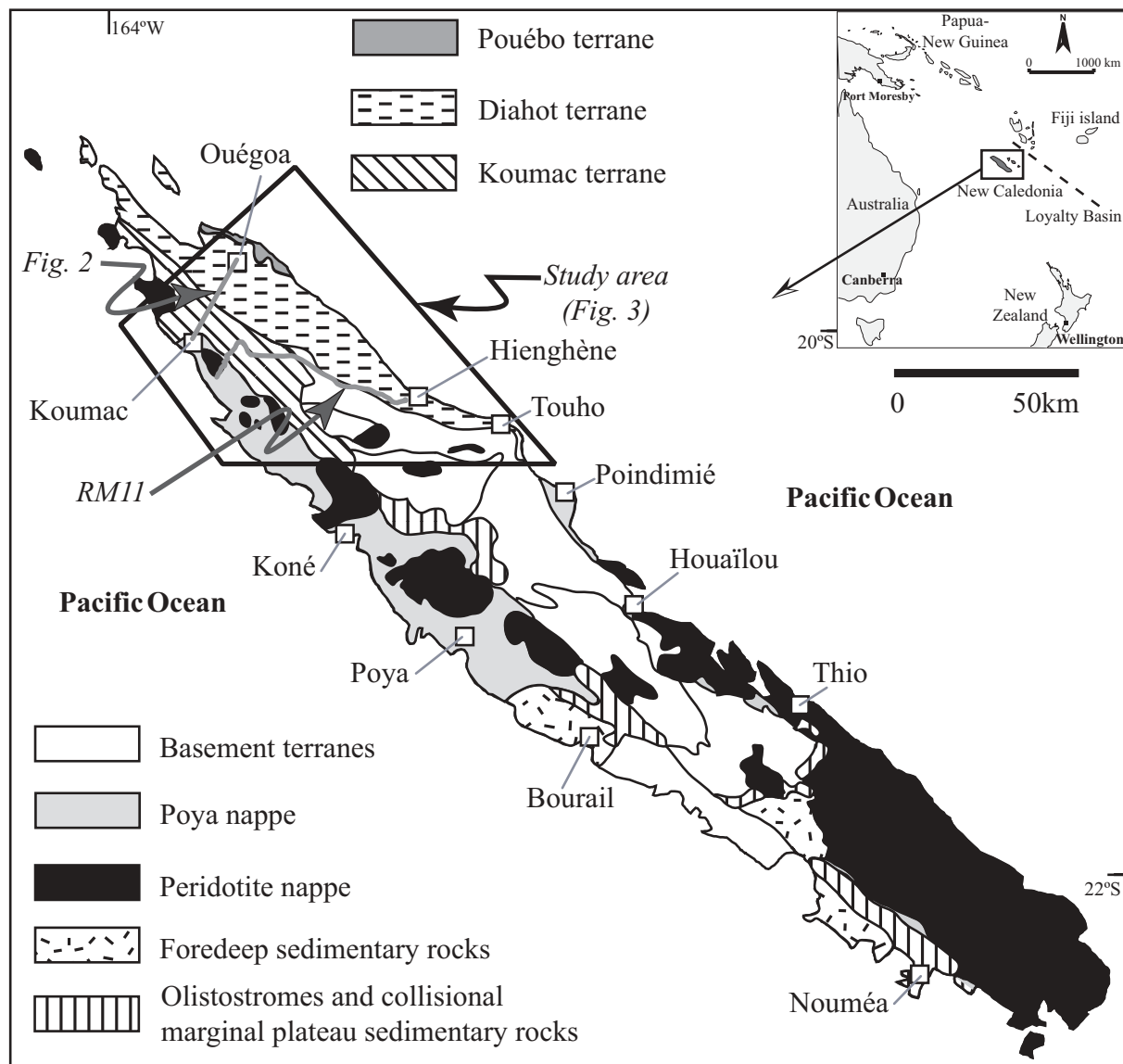
Fig. 1. Structural map of New Caledonia showing the major tectonic units, after Cluzel *et al.* (1994) and Fitzherbert *et al.* (2003). The inset shows the location of New Caledonia in the SW Pacific. The Koumac–Ouégoa road and RM11 road profiles are indicated (pale grey continuous lines).

from diagenesis to very low-grade metamorphism, because vitrinite reflectance increases irreversibly with temperature, and retains an indication of the maximum paleo-temperature (Teichmüller, 1987; Ferreiro Mählmann, 2001). Organic maturity is not controlled by starting material, oxygen fugacity–water activity (Ernst & Ferreiro Mählmann, 2004) and temperature–time (Teichmüller, 1987), and is independent of host lithology. A review of the literature shows, however, that field observations and experimental data display inconsistencies when the effects of pressure on vitrinite maturation are considered. For example, in the Diablo Range (Franciscan Complex, California), Dalla Torre *et al.* (1994, 1996*a*) demonstrated that the maturation of

organic matter was lower than expected, compared with both the illite crystallinity and the metamorphic grade determined through the mineral assemblages. They attributed the abnormally low vitrinite reflectance values to the effect of pressure based on field evidence described by Goffé & Velde (1984), Feldhoff *et al.* (1991), Fang & Jiaynu (1992) and Ferreiro Mählmann (1994). This model was subsequently corroborated by an experimental study on the pressure dependence of vitrinite maturation (Dalla Torre *et al.*, 1997). Based on this work and new experiments, Ernst & Ferreiro Mählmann (2004) proposed a thermobarometric application of vitrinite reflectance based on a kinetic model. The problem in poly-metamorphic areas
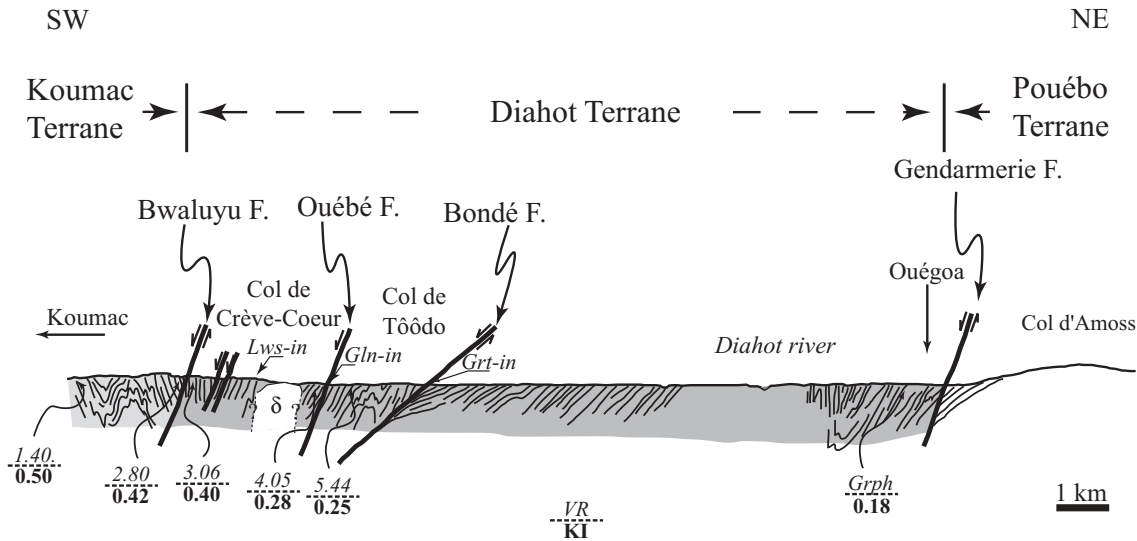
Fig. 2. Schematic cross-section between Koumac and Ouégoa modified after Rawling & Lister (1999). Average values of Kübler index (KI) are indicated in bold and average vitrinite reflectance values (VR; after Diessel *et al.*, 1978) in italics. The symbol δ indicates the presence of diabase. Mineral abbreviations are those of Kretz (1983).

such as the Vanoise in the French Alps (Goffé & Velde, 1984), the Tripolitza Series in Greece (Feldhoff *et al.*, 1991), the Arosa Zone in the European Alps (Ferreiro Mählmann, 1994) and the Diablo Range in the Franciscan Complex (Dalla Torre *et al.*, 1997) is that no coherent relationship between organic and inorganic parameters for determining the metamorphic grade has been identified.

This contribution summarizes the results of our investigation of the very low-grade metapelites of the Koumac and Diahot terranes in New Caledonia, using the illite crystallinity and *b* cell dimensions of K-white micas, together with thermodynamic modeling of Al-rich metapelites and fluid inclusion measurements. The determination of the *b* cell dimension of K-white mica and fluid inclusion barometry of syn-metamorphic vein minerals, together with the use of vitrinite reflectance, provided an excellent opportunity to determine the effect of pressure on vitrinite reflectance in very low- to low-temperature domains. The results are compared with the existing vitrinite reflectance measurements for this area (Diessel *et al.*, 1978) and oxygen thermometry studies (Black & Brothers, 1977), to compare the evolution of illite crystallinity and vitrinite reflectance in an HP metamorphic belt. The maximum pressure and temperature metamorphic conditions in the Diahot terrane based on previous studies (Black & Brothers, 1977; Bell & Brothers, 1985) are similar to those observed in the Tripolitza Series and the Diablo Range. This metamorphic belt provides a rare natural laboratory to test the experimentally observed pressure retarding effects on vitrinite reflectance recorded by Dalla Torre *et al.* (1997), by studying metapelites from a high-pressure metamorphic schist belt.

REGIONAL GEOLOGY

New Caledonia is a dispersed fragment of the eastern margin of Gondwana resulting from the opening of the Tasman Sea and rifting of New Caledonia and New Zealand from Australia. In Late Eocene time, the New Caledonian fragment collided with an intraoceanic island-arc system (Cluzel *et al.*, 1994, 2001; Aitchison *et al.*, 1995; Clarke *et al.*, 1997), and a NE-facing subduction system was established beneath the Loyalty Basin. The collision, responsible for the main deformation of the continental basement of New Caledonia, generated an HP schist belt coeval with the southwestwards thrusting of two nappes over the basement. The Poya nappe or 'formation des basalts' (Paris, 1981) is a mafic sheet overlying all the pre-Neogene tectonic units (Fig. 1), comprising dolerite, tectonized tholeiitic pillow basalts and abyssal argillites. The peridotite nappe is an ophiolite complex that initially covered much of the island; faulting and erosion has removed much of it, but it still dominates outcrops in the south of the island. The basement is composed of terranes of Palaeozoic to Mesozoic age of varying metamorphic grade, transgressively overlain by upper Cretaceous to Eocene sedimentary rocks deposited during Gondwana dispersal (Aitchison *et al.*, 1995; Clarke *et al.*, 1997).

Post Early Cretaceous tectonic units (Figs 1 and 2) include the Poya and peridotite nappes and the Koumac, Diahot and Pouébo basement terranes. The Koumac terrane (Cluzel *et al.*, 1994) is a part of the olistrostrome and collisional marginal plateau sedimentary terrane of Fitzherbert *et al.* (2003). It consists of an intensively tectonized Late Cretaceous to Early Eocene
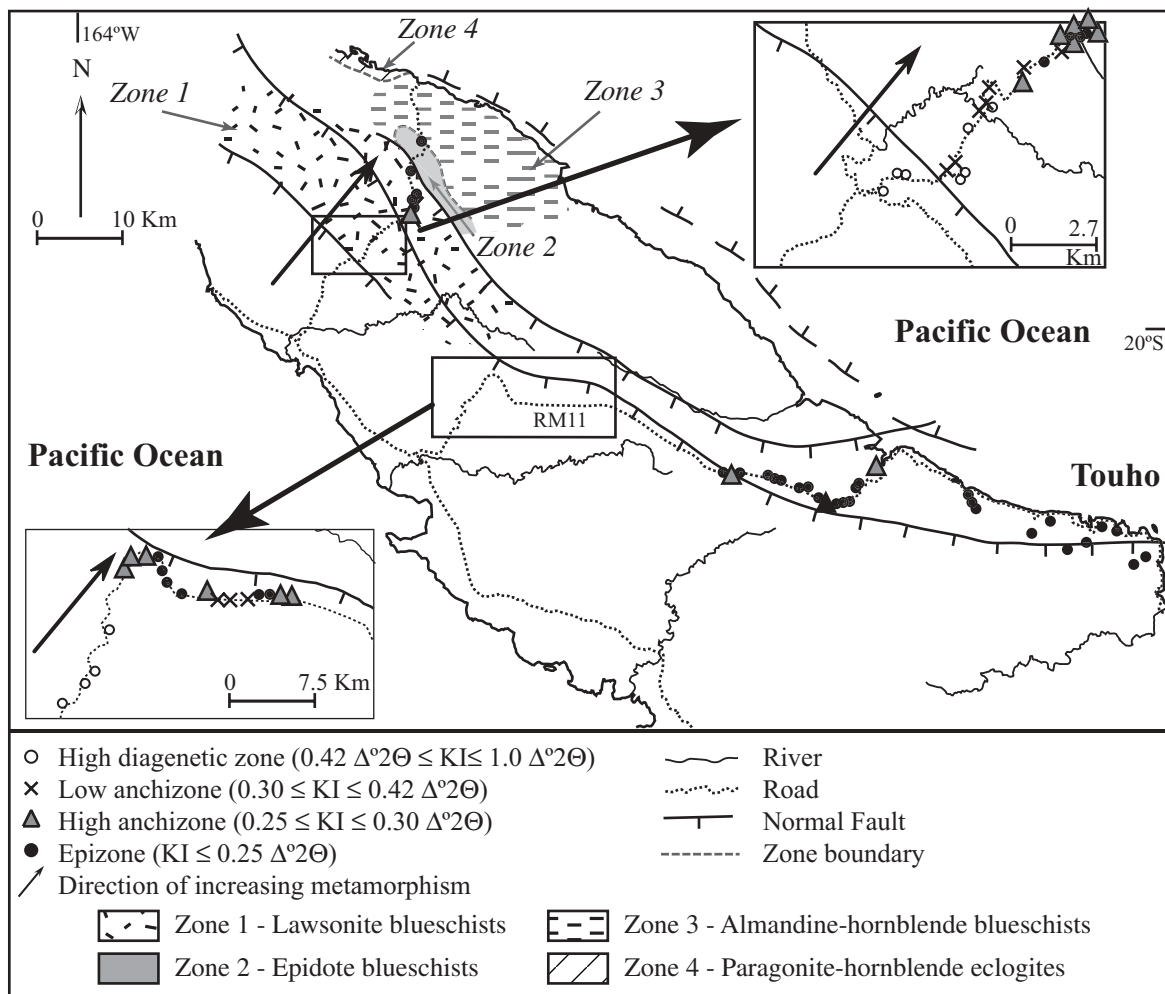
Fig. 3. Distribution of Kübler index (KI) values in the study area. Metamorphic zones 1–4 (see text) from Fitzherbert *et al.* (2003) are indicated.

sequence of flysch, chert, limestone and black shale. The Diahot terrane contains an interbedded sequence of Cretaceous to Eocene metasediments and felsic volcanics metamorphosed under high-P/T conditions (Fitzherbert *et al.*, 2003). The easternmost terrane is the Pouébo terrane; a mélange containing large mafic eclogite boulders enclosed in an argillaceous or serpentine-rich matrix (Maurizot *et al.*, 1989). $^{40}Ar/^{39}Ar$ dating of white micas from the Diahot and Pouébo units yielded consistent Middle to Late Eocene cooling ages of $37 \pm 1\,Ma$ (Ghent *et al.*, 1994). Metamorphism is bracketed between the Early Eocene (youngest sediments) and Late Eocene (cooling ages).

This study is focused on the Koumac and Diahot terranes (Figs 1–3). The Koumac terrane includes the lowest-grade metasediments of the high-pressure belt as defined by the presence of pumpellyite and prehnite in basic igneous rocks (Brothers, 1974; Black, 1977). In this terrane vitrinite reflectance is $2\cdot9\%\ R_{max}$ and the

maximum pressure and temperature were $0\cdot3\,GPa$ and $250°C$ (Diessel *et al.*, 1978). Fitzherbert *et al.* (2003) subdivided the Diahot terrane into four zones based on the metabasite mineral assemblage (Fig. 3): (1) lawsonite blueschists ($P = 1\cdot0\,GPa$ and $T = 400°C$); (2) epidote blueschists ($P = 1\cdot4$–$1\cdot5\,GPa$ and $T = 450$–$500°C$); (3) almandine–hornblende blueschists ($P = 1\cdot4$–$1\cdot6\,GPa$ and $T = 550$–$580°C$); (4) paragonite–hornblende eclogites ($P = 1\cdot7\,GPa$ and $T = 600$–$620°C$). Our study area in the Diahot unit is limited to the region to the SW of the Gendarmerie fault (Fig. 2), equivalent to Zone 1 (lawsonite blueschist) of Fitzherbert *et al.* (2003).

MATERIAL AND METHODS

Eighty-six samples of metapelite and 11 meta-marls (Table 1) were collected from the Koumac and Diahot terranes (Fig. 3). In northern New Caledonia outcrops are

Table 1: Geographical location, rock type and mineralogy of the studied samples

Sample	Latitude	Longitude	Alt. (m)	Rock type	Qtz	Ab	KWM	Chl	Pg	Kln	Stp	I/S	C/S	K/S	Lws	Gln	Others	Terrane
Koumac—Ouégoa profile																		
MF2989	20°30′15″	164°16′26″	48	marl	*	*	*				*						Hem	Koumac
MF2992	20°27′59″	164°19′58″	60	marl	*		*			*							Hem	Koumac
MF2994	20°27′49″	164°20′02″	80	marl	*		*	*		*							Hem	Koumac
MF2995	20°27′50″	164°20′36″	100	pelite	*		*			*							Hem	Koumac
MF2996	20°27′42″	164°21′08″	100	pelite	*		*	*										Koumac
MF3008	20°27′48″	164°21′12″	100	marl	*		*	*									Cor	Koumac
MF3009	20°27′48″	164°21′12″	100	marl	*	*	*	*									Vm	Koumac
MF2997	20°27′38″	164°21′14″	90	marl	*	*	*	*									Cor	Koumac
MF2998	20°26′59″	164°21′34″	110	pelite	*		*	*	*				*					Koumac
MF2999	20°26′40″	164°21′46″	120	pelite	*		*			*				*				Koumac
MF3000	20°26′29″	164°21′44″	120	pelite	*		*			*				*				Koumac
MF3001	20°26′38″	164°22′06″	120	pelite	*	*	*	*	*									Koumac
MF3002	20°26′23″	164°22′12″	140	pelite	*		*			*								Koumac
MF3003	20°26′10″	164°22′22″	180	pelite	*	*	*	*					*					Koumac
MF3005	20°26′08″	164°22′28″	200	pelite	*	*	*	*					*		*			Diahot
MF3007	20°25′58″	164°22′49″	205	pelite	*	*	*						*					Diahot
MF3014	20°25′58″	164°22′49″	205	pelite	*	*	*	*										Diahot
MF3017	20°25′55″	164°22′51″	180	pelite	*	*	*	*	*				*					Diahot
MF3018	20°25′55″	164°22′51″	180	pelite	*	*	*	*	*									Diahot
MF3020	20°25′40″	164°23′02″	130	pelite	*	*	*		*				*					Diahot
MF3024	20°25′37″	164°23′20″	100	pelite	*	*	*	*	*				*	*	*			Diahot
MF3025	20°25′34″	164°23′24″	80	pelite	*	*	*		*					*				Diahot
MF3026	20°25′53″	164°23′29″	60	marl	*	*	*	*							*			Diahot
MF3027	20°25′33″	164°23′29″	60	pelite	*	*	*	*							*			Diahot
MF3028	20°25′12″	164°24′03″	60	pelite	*	*	*							*	*			Diahot
PS89	20°25′12″	164°24′03″	60	pelite	*		*	*	*								Carp	Diahot
MF3029	20°24′51″	164°24′07″	80	pelite	*	*	*							*	*	*		Diahot
MF3030	20°23′49″	164°24′29″	20	pelite	*	*	*							*	*	*		Diahot
MF3031	20°23′33″	164°24′35″	20	pelite	*	*	*	*							*	*		Diahot
PS131	20°22′11″	164°25′02″	20	pelite	*	*	*	*							*	*		Diahot
MF3070	20°21′49″	164°25′13″	10	pelite	*	*	*			*				*		*		Diahot
MF3071	20°20′31″	164°25′15″	50	pelite	*		*		*	*				*				Diahot
Touho region																		
PS11	20°43′51″	165°01′29″	20	pelite	*	*	*	*										Diahot
PS12	20°44′11″	165°00′52″	20	pelite	*	*	*	*						*				Diahot
PS13	20°44′26″	165°00′15″	25	pelite	*	*	*	*		*								Diahot
PS14	20°46′50″	165°06′20″	40	pelite	*	*	*	*										Diahot
PS15	20°47′02″	165°06′01″	40	pelite	*	*	*	*										Diahot
PS16	20°41′50″	164°44′14″	400	pelite	*	*	*	*									Ep	Diahot
PS29	20°47′36″	165°08′32″	20	pelite	*	*	*	*							*			Diahot
PS30	20°47′40″	165°08′05″	10	pelite	*	*	*	*		*					*			Diahot
PS31	20°46′57″	165°10′41″	2	pelite	*	*	*	*							*			Diahot
PS32	20°47′55″	165°13′59″	460	pelite	*	*	*	*		*								Diahot
PS33	20°48′03″	165°13′30″	350	pelite	*	*	*	*		*								Diahot
PS36	20°57′09″	165°19′48″	10	pelite	*	*	*	*					*		*			Diahot
PS37	20°58′30″	165°20′52″	80	pelite	*	*	*	*		*								Diahot
PS54	21°02′08″	165°21′02″	5	pelite	*		*	*										Diahot
PS55	21°02′28″	165°20′54″	20	pelite	*	*	*	*										Diahot
PS56	21°02′33″	165°21′56″	5	pelite	*	*	*	*										Diahot
PS57	21°00′02″	165°19′58″	20	pelite	*	*	*	*		*								Diahot

Table 1: Continued

Sample	Latitude	Longitude	Alt. (m)	Rock type	Qtz	Ab	KWM	Chl	Pg	Kln	Stp	I/S	C/S	K/S	Lws	Gln	Others	Terrane
Profile along the RM11																		
MF3034	20°38′59″	164°26′51″	40	pelite	*	*						*			*		Cor	Koumac
MF3035	20°38′15″	164°27′13″	240	marl	*	*	*					*						Koumac
MF3036	20°37′52″″	164°27′38″	320	marl	*	*	*					*	*					Koumac
MF3037	20°37′48″	164°27′40″	340	marl	*	*	*					*	*					Koumac
MF3038	20°37′08″	164°27′55″	200	pelite	*					*		*						Koumac
MF3039	20°36′42″	164°28′13″	240	pelite	*					*		*						Koumac
MF3040	20°36′33″	164°28′21″	300	pelite	*		*			*								Koumac
MF3041	20°36′10″	164°28′22″	320	pelite	*		*			*	*							Koumac
MF3042	20°35′56″	164°28′59″	400	pelite	*	*	*			*	*							Koumac
MF3043	20°35′52″	164°29′26″	380	pelite	*	*	*			*	*							Koumac
MF3044	20°35′35″	164°30′03″	260	pelite	*	*	*	*	*					*				Koumac
MF3051	20°35′31″	164°30′36″	300	pelite	*	*	*	*	*			*					Cor	Diahot
MF3052	20°35′30″	164°30′40″	180	pelite	*	*	*	*	*						*			Diahot
MF3053	20°35′10″	164°31′16″	100	pelite	*	*	*	*	*			*	*					Diahot
MF3054	20°35′55″	164°31′23″	120	pelite	*	*	*	*					*					Diahot
MF3055	20°36′09″	164°31′40″	140	pelite	*	*	*	*					*		*			Diahot
MF3056	20°36′20″	164°32′12″	120	pelite	*	*	*	*	*				*		*			Diahot
MF3057	20°36′30″	164°32′58″	140	pelite	*	*	*	*	*					*				Diahot
MF3058	20°36′28″	164°33′42″	130	pelite	*	*	*		*	*								Diahot
MF3059	20°36′31″	164°33′57″	130	pelite	*	*	*	*	*									Diahot
MF3060	20°36′31″	164°34′00″	130	pelite	*	*	*	*	*									Diahot
MF3061	20°36′26″	164°34′29″	160	marl	*	*	*	*	*									Diahot
MF3062	20°36′18″	164°35′09″	300	pelite	*		*			*	*							Koumac
MF3063	20°36′18″	164°35′41″	340	pelite	*	*	*			*	*							Koumac
MF3064	20°36′18″	164°36′10″	400	pelite	*	*	*			*	*							Koumac
MF3065	20°36′19″	164°36′35″	440	pelite	*		*	*	*									Diahot
MF3067	20°36′51″	164°37′12″	400	pelite	*		*	*	*						*			Diahot
MF3068	20°37′09″	164°38′12″	300	pelite	*	*	*		*								Cor	Diahot
PS24	20°40′01″	164°41′53″	360	pelite	*	*	*	*							*			Diahot
PS23	20°40′18″	164°42′35″	500	pelite	*	*	*	*	*									Diahot
PS22	20°40′48″	164°43′03″	600	pelite	*	*	*	*			*							Diahot
PS21	20°41′58″	164°43′03″	480	pelite	*	*	*	*										Diahot
PS20	20°41′00″	164°43′29″	500	pelite	*	*	*	*			*				*			Diahot
MF3154	20°46′35″	164°45′20″	460	pelite	*	*	*	*	*						*			Diahot
MF3153	20°46′38″	164°45′41″	360	pelite	*	*	*	*							*	*		Diahot
MF3152	20°46′41″	164°46′19″	140	pelite	*	*	*	*							*			Diahot
MF3151	20°47′51″	164°47′48″	160	pelite	*		*	*	*									Diahot
MF3149	20°48′12″	164°49′23″	20	pelite	*		*	*	*									Diahot
MF3148	20°48′11″	164°49′51″	5	pelite	*	*	*	*			*							Diahot
MF3147	20°48′59″	164°51′12″	40	pelite	*	*	*	*							*			Diahot
MF3146	20°49′21″	164°51′57″	30	pelite	*	*	*	*			*				*			Diahot
MF3145	20°49′26″	164°52′24″	20	pelite	*	*	*	*			*				*		Ep	Diahot
MF3144	20°49′15″	164°53′12″	40	pelite	*	*	*	*			*				*			Diahot
MF3143	20°49′10″	164°53′46″	20	pelite	*	*	*	*							*			Diahot
MF3142	20°48′42″	164°54′22″	20	pelite	*	*	*	*				*	*					Diahot
MF3141	20°48′32″	164°54′18″	40	pelite	*	*	*	*				*	*					Diahot
MF3140	20°48′02″	164°55′38″	20	pelite	*	*	*	*					*		*			Diahot
MF3139	20°47′22″	164°55′59″	40	pelite	*	*	*	*			*		*		*			Diahot

Mineral abbreviations are from Kretz (1983); except: KWM, K-white micas (illite, muscovite); I/S, illite/smectite; C/S, chlorite/smectite; K/S, kaolinite/smectite; Vm, vermiculite; Cor, corrensite.

poor because of extensive tropical weathering, limiting the availability of fresh samples mainly to road cuts. Therefore, samples were collected only along two road profiles (Koumac–Ouégoa and road RM11) and along various small paths (Touho region) (Fig. 3). In many common rock types, such as marine pelites and carbonates, no diagnostic minerals or mineral assemblages form in the very low-grade field. In these rocks the transitions from non-metamorphic to very low-grade and from very low-grade to low-grade metamorphic domains take place through the diagenetic zone, the anchizone and the epizone, each zone being characterized by specific values of the illite Kübler Index (KI) (Árkai *et al.*, 2003).

Clay mineral separation was conducted using techniques described by Schmidt *et al.* (1997). To perform the illite–muscovite polytype determination, randomly oriented samples were prepared using the technique described by Dalla Torre *et al.* (1994).

X-ray diffraction

Illite and chlorite crystallinity was measured on air-dried, glycolated and heated samples using a D5000 Bruker-AXS (Siemens) diffractometer, CuKα radiation at 40 kV and 30 mA, and automatic divergence slits (primary and secondary V20) with a secondary graphite monochromator.

Illite crystallinity was calculated using the software DIFFRAC^{Plus} TOPAS (by ©Bruker AXS). The illite crystallinity index is defined as the full width at half maximum (FWHM) intensity of the first illite–muscovite basal reflection (Table 2). Illite crystallinity values were transformed into Kübler index (KI) values using a correlation with the standard samples of Warr & Rice (1994) ($KI_{CIS} = 1.343 \times IC_{Basel} - 0.003$). The Kübler index was used to define the limits of metamorphic zones, and the transition values were chosen as follows: $KI = 0.25 \Delta°2\Theta$ for the epizone to high anchizone boundary, $KI = 0.30 \Delta°2\Theta$ for the high to low anchizone boundary and $KI = 0.42 \Delta°2\Theta$ for the low anchizone to diagenetic zone. The same experimental conditions were also used to determine chlorite crystallinity on the (002) peak, where (ChC(002)) corresponds to the FWHM intensity values of the second (7 Å) basal reflection of chlorite (Table 2). The ChC(002) measurements were calibrated with those of Warr & Rice (1994) and expressed as the Árkai index (ÁI) (Guggenheim *et al.*, 2002): $ÁI = 0.766 \times ChC(002) + 0.117$. The anchizone boundaries for the Árkai index were defined by correlation with the Kübler index and are given as $0.24 \Delta°2\Theta$ for the epizone to anchizone boundary and $0.30 \Delta°2\Theta$ for the anchizone to diagenetic zone.

The different types of mixed-layer clay minerals observed were classified using data from Moore & Reynolds (1997). The illite/smectite glycolated mixed-layer clay minerals were identified on the diffractogram by the presence of a reflection between 16 and 17·7 $\Delta°2\Theta$. After glycolation solvation, the chlorite/smectite was identified by expansion of the $d(001)*$ to 31·1 Å. Heat treatment was necessary for identification of the kaolinite/smectite. Heating produces a shift from the 7·4 Å air-dried reflection to an increased d value of 8·1 Å.

K-white mica b cell dimensions (or b cell dimensions) were determined for samples free of paragonite and mixed-layered minerals. The b cell dimension is based on the $d_{060,331}$ spacing and on the increasing celadonite substitution that occurs with pressure increase in white mica (Ernst, 1963; Guidotti *et al.*, 1989). Guidotti *et al.* (1989) presented linear regression equations that quantify the changes in the b cell dimensions of muscovite $2M_1$ that result from cation substitutions in the interlayer and octahedral sites. This b cell dimension value was determined by measurement of the (060) peak of the potassic white mica when present (Sassi & Scolari, 1974), and using the program WIN-METRIC V.3.0.7 (by ©Bruker AXS), which is a cell-refinement program.

Electron microprobe and X-ray fluorescence data

Mineral compositions in the metapelites were determined by electron probe microanalysis using a JEOL JXA-8600 superprobe at the University of Basel with four wavelength-dispersive spectrometers, equipped with Voyager software by NORAN instruments. A ZAF-type correction procedure was used for all data reduction and all Fe was assumed to be ferrous. To avoid volatilization of light elements, low-grade metamorphic minerals were analyzed using a 10 nA beam current, an accelerating voltage of 15 kV, an acquisition time of 10 or 20 s, rastered over an area of 26 μm^2. The standards used for the elements were as follows: olivine for Si and Mg; rutile for Ti; gehlenite for Al; graftonite for Mn and Fe; wollastonite for Ca; albite for Na; and orthoclase for K.

Two whole-rock chemical analyses were made at the Geochemistry Laboratories, University of Basel. Major oxide concentrations were measured on a fused glass bead (20 mm diameter) containing a mixture of 300 mg sample powder and 4700 mg Li-tetraborate. The two analyses (Table 3) were obtained with a Siemens SRS3000 Wavelength-Dispersive Sequential X-Ray Spectrometer with a Rh end window tube (4 kV). The results were collected and evaluated using the Bruker AXS Spectra plus standardless evaluation program. Analytical precision varies from element to element, as do detection limits, but generally the major oxides have a detection limit of 0·01% and a relative accuracy of 0·5%.

Table 2: FWHM and ChC(002) data of the studied samples

Sample	FWHM	ChC(002)
Koumac−Ouégoa profile		
MF2989	1·74	—
MF2992	0·40	—
MF2994	0·33	—
MF2995	0·39	—
MF2996	0·31	0·21
MF3008	0·34	0·22
MF3009	0·39	Weat.
MF2997	0·30	0·18
MF2998	0·32	—
MF2999	0·54	—
MF3000	0·25	—
MF3001	Int.	0·31
MF3002	0·24	—
MF3003	0·35	0·30
MF3005	0·27	0·23
MF3007	0·23	Weat.
MF3014	0·20	0·18
MF3017	0·25	0·18
MF3018	0·22	0·17
MF3020	0·21	Weat.
MF3024	0·20	Weat.
MF3025	0·21	Weat.
MF3026	0·23	0·19
MF3027	0·17	0·16
MF3028	0·21	Weat.
PS89	—	—
MF3029	0·19	Weat.
MF3030	0·20	Weat.
MF3031	0·17	Weat.
PS131	—	—
MF3070	0·16	Weat.
MF3071	0·15	Weat.
Touho region		
PS11	0·17	Weat.
PS12	0·15	Weat.
PS13	0·17	0·17
PS14	0·14	0·16
PS15	0·18	0·17
PS16	0·18	0·19
PS29	0·14	0·14
PS30	0·16	0·16
PS31	0·17	0·16
PS32	0·18	0·16
PS33	0·18	0·16
PS36	0·18	Weat
PS37	0·14	0·14
PS54	0·19	0·17
PS55	0·15	0·15
PS56	0·20	0·18
PS57	0·22	0·19

Sample	FWHM	ChC(002)
Profile along the RM11		
MF3034	—	—
MF3035	0·48	—
MF3036	1·32	—
MF3037	0·43	—
MF3038	1·97	—
MF3039	1·36	—
MF3040	1·21	—
MF3041	1·05	—
MF3042	0·75	—
MF3043	0·44	—
MF3044	0·45	—
MF3051	0·26	Weat.
MF3052	0·22	0·18
MF3053	0·15	0·13
MF3054	0·17	0·11
MF3055	0·17	0·12
MF3056	0·28	0·17
MF3057	0·24	0·31
MF3058	0·23	—
MF3059	0·23	0·15
MF3060	0·24	0·19
MF3061	0·24	0·19
MF3062	0·67	—
MF3063	0·32	0·26
MF3064	0·38	0·28
MF3065	0·22	0·19
MF3067	0·28	0·48
MF3068	0·23	0·20
PS24	0·17	0·15
PS23	0·21	Weat.
PS22	0·17	0·16
PS21	0·27	0·18
PS20	0·21	0·18
MF3154	0·22	0·21
MF3153	0·20	0·19
MF3152	0·23	0·20
MF3151	0·19	0·19
MF3150	0·21	0·20
MF3149	0·23	0·19
MF3148	0·19	0·17
MF3147	0·15	0·11
MF3146	0·14	0·13
MF3145	0·22	0·19
MF3144	0·14	0·14
MF3143	0·14	Weat.
MF3142	0·13	0·21
MF3141	0·12	0·17
MF3140	0·15	Weat.
MF3139	0·20	Weat.

FWHM, full width at half maximum intensity of the (001) illite−muscovite reflection. Weat., weathering; Int, interference with another peak.

Table 3: Whole-rock compositions of samples used for thermodynamic modeling

Oxides (wt %)	MF3031	MF2994
SiO$_2$	50·74	90·02
TiO$_2$	1·08	0·20
Al$_2$O$_3$	21·03	5·00
FeO	5·52	1·54
MnO	0·35	0·00
MgO	2·34	1·02
CaO	0·84	0·00
Na$_2$O	2·70	0·00
K$_2$O	7·15	0·85
P$_2$O$_5$	0·43	0·10
LOI	7·56	1·19
Fe/(Fe + Mg)	0·70	0·60

LOI, loss on ignition.

Thermodynamic modeling

Pressure and temperature conditions of equilibrium of the metamorphic rocks were determined by calculating equilibrium assemblages and equilibrium phase diagrams using the THERIAK-DOMINO software (de Capitani & Brown, 1987; de Capitani, 1994). A modified internally consistent mineral database based on JUN92 of Berman (1988) was supplemented with thermodynamic data for ferro- and magnesio-carpholite, and magnesio- and ferro-chloritoid from Le Bayon (2002). Data for glaucophane and ferro-glaucophane (El-Shazly & Liou, 1991), daphnite and phengite (Massonne & Szpurka, 1997) were also added. The activity models are presented in Table 4. The main input consists of the bulk-rock composition of the rock studied.

Microthermometry

Quartz–calcite veins were sampled along the road between Koumac and Ouégoa (Fig. 3), to substantiate the *P–T* estimations based on mineral equilibria and to reconstruct the fluid evolution history during metamorphism (Frey *et al.*, 1980). Microthermometry investigations on double polished thin sections were performed using a Chaixmeca heating–freezing stage at the University of Basel (Poty *et al.*, 1976; Mullis *et al.*, 1994). The uncertainty of the measurements is $\pm 0{\cdot}1°C$ for -60 to $40°C$ and $\pm 1°C$ outside this range.

Two-phase (consisting of vapor and liquid at room temperature) and one-phase fluid inclusions were identified. No dissolved volatile phase was observed, either by melting of CO$_2$ at or below its triple point of $-56{\cdot}6°C$, nor by formation or dissociation of a clathrate

Table 4: Solution model used for thermodynamic modeling

Epidote–clinozoisite: ideal one site mixing

$a_{Ep} = X_{Fe}^{M}$

$a_{Czo} = X_{Al}^{M}$

Chlorite: ideal one site mixing

$a_{Daph} = X_{Fe}^{5}$

$a_{Clin} = X_{Mg}^{5}$

Glaucophane: ideal one site mixing

$a_{Fe-Gln} = X_{Fe}^{3}$

$a_{Mg-Gln} = X_{Mg}^{3}$

or liquid–vapor equilibrium of a volatile component such as higher hydrocarbons (HHC), CH$_4$, CO$_2$, N$_2$ or H$_2$S. Thus, microthermometry was restricted to measuring the eutectic temperature (T_e), the melting temperature of ice (Tm_{ice}) and the bulk homogenization temperature of the fluid inclusions (Th_I). The eutectic temperature provides evidence for the composition of the electrolytes dissolved in aqueous solutions (Hollister & Crawford, 1981; Shepherd *et al.*, 1985; Mullis, 1987). As none of the investigated fluid inclusions contained any observable gas component, salinity was derived from the ice melting temperature in NaCl-equivalence after Potter *et al.* (1978). Bulk homogenization temperatures of gas-free aqueous solutions were used for the determination of the volume fraction of the vapor and liquid phases after Zhang & Frantz (1987).

From the salinity and volume fraction of vapor and liquid phases within the fluid inclusions, bulk density and inclusion composition were calculated according to the general equations published by Mullis (1987). The isochors were calculated from the equation of state given by Zhang & Frantz (1987).

RESULTS
Mineralogy

The mineralogy of the studied samples is given in Table 1. Minerals abbreviations are those of Kretz (1983).

In the meta-marls, the mineral assemblages consist of Qtz + K-white mica + Kln and/or Chl with minor amounts of mixed-layer minerals [illite/smectite (I/S), and chlorite/smectite (C/S)], albite, and sporadically hematite. In their $<2\,\mu m$ grain-size fraction, illite–muscovite predominates in association with Chl or Kln, mixed-layer minerals and quartz. Albite is present in only minor amounts, and vermiculite (Vm) and corrensite (Cor) are found in few samples.

In the metapelites, the mineral assemblages consist of Qtz, K-white mica, Chl and/or Kln with minor amounts of mixed-layer minerals [I/S, C/S and kaolinite/smectite
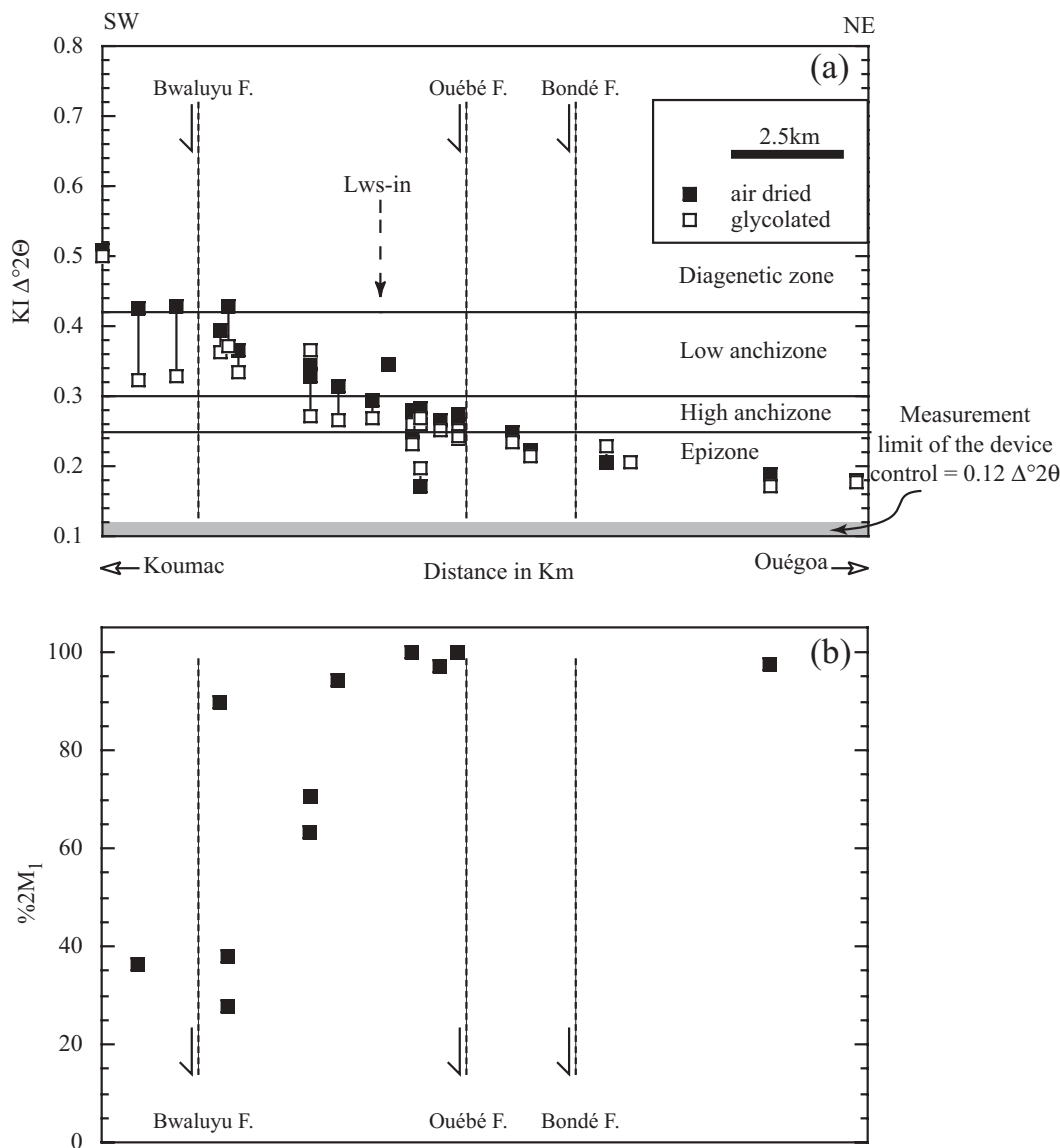
Fig. 4. (a) Distribution patterns of KI (air-dried and glycolated) as a function of distance along the Koumac–Ouégoa profile. (b) $2\,M_1$% K-white mica content of samples along the Koumac–Ouégoa road.

(K/S)], Ab, and index minerals depending on the metamorphic grade (stilpnomelane, lawsonite, glaucophane, carpholite, epidote). In their $<2\,\mu m$ fractions, illite–muscovite or phengitic muscovite predominate in the higher-grade samples. Discrete paragonite is also found in minor quantities. Traces of smectite or kaolinite indicate oxidative weathering in some higher-grade samples.

Structural characteristics of the phyllosilicates

Figures 2 and 3 show the distribution of the illite crystallinity (KI data) and the FWHM values are presented in Table 2.

The KI values range from low diagenetic to epizone. In the Koumac terrane, the KI data indicate low diagenetic to low anchizone values, ranging from 1·40 to 0·33 $\Delta°2\Theta$. In the Diahot terrane, KI values vary between low anchizone and epizone. A trend of increasing grade from the diagenetic zone to the epizone is observed in a traverse from SW to NE along the Koumac–Ouégoa road (Figs 1, 2 and 4a). An overall prograde sequence for the terranes is documented, with KI decreasing from SW to NE.

Significant positive linear correlation ($r^2 = 0·65$) is found between Kübler and Árkai indices (Fig. 5), giving greater reliability to the metamorphic grade estimate deduced from KI values, which can be hindered by

y = 0.17386 + 0.27794x
R² = 0.65
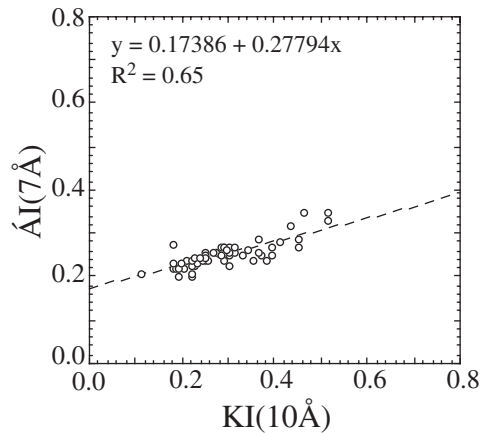
Fig. 5. Correlation between KI (10 Å) and ÁI (7 Å) values.

broadening of the reflectance peak caused by the presence of discrete paragonite.

The percentage of $2\,M_1$ illite–muscovite polytype relative to the KI along the Koumac–Ouégoa road shows a positive trend with increasing metamorphic grade (Fig. 4b). The complete conversion from $1\,M_d$ to $2\,M_1$ is reached at KI values around $0{\cdot}30\,\Delta°2\Theta$ (limit of the low to high anchizone; Table 5).

The K-white mica b cell dimension for 20 K-white mica samples from the lawsonite and glaucophane zones all fall in the same range with a minimum 9·04 and a maximum 9·06 Å values. Eight samples from the pumpellyite–prehnite zone show lower values between 9·01 and 9·03 Å (Fig. 6). The b values from the glaucophane–lawsonite zone are typical for HP-type metamorphism, whereas the prehnite–pumpellyite values are more characteristic of Barrovian-type metamorphism (Sassi, 1972; Sassi & Scolari, 1974).

Mineral chemistry

Phyllosilicate chemistry

Because of the small grain size of the phyllosilicates, special care was taken to differentiate between detrital and newly formed metamorphic grains. In certain cases (i.e. MF3003), detrital micas altered to K-white mica/chlorite or K-white mica/paragonite/chlorite stacks were observed. They could be distinguished from fine-grained, matrix-forming white mica and chlorite formed parallel to the metamorphic schistosity.

Representative compositions of K-white mica are listed in Table 6. Mica analyses showing more than 0·5% (MnO % + TiO$_2$ %) were rejected (Vidal & Parra, 2000). In a Si–Al$_{tot}$ diagram (Fig. 7a), the analyses show a significant deviation from the Tschermak exchange line. Considering the analyses reported in Table 6, the total interlayer charge (t.i.c. = Ca + Na + 2K) is between 1 and 0·90, except for sample MF3144, where a Prl

substitution could be assumed (Fig. 7a and d) in addition to the Tschermak substitution. Additional substitutions are required to explain the excess of Fe and Mg (Fig. 7a and b). The excess of Mg + Fe could be explained by a di–trioctahedral substitution common in dioctahedral micas (Vidal & Parra, 2000; Parra *et al.*, 2002). Figure 7c shows a correlation between the Fe and Mg contents in the individual samples (probably dependent on the bulk composition) except for samples PS56 and PS32. On the basis of model calculations supposing various mixtures (Fig. 7b), no contamination of the analyses by quartz or chlorite has occurred.

In Fig. 7d, the K-white mica analyses fall in a cluster between the muscovite–phengite and the muscovite–illite lines, indicating a small deficit in t.i.c. (values range between 0·8 and 0·95 p.f.u.). Figure 7e shows that the Na content of K-white mica is very low (except for samples MF3003 and PS89) and thus the b cell dimension is not influenced by K–Na exchange. Therefore use of the b cell dimension should be accurate (Guidotti *et al.*, 1989).

Although the number of data pairs is relatively low ($n = 6$), we investigated the relation between the metamorphic grade of our samples and the chemistry of the K-white micas. No real trend is observed between Na/(Na + K) ratio and metamorphic grade, as indicated by KI value (Fig. 7f), suggesting that subordinate amounts of discrete paragonite and/or mixed K/Na micas do not influence the KI. Figure 7g reveals no obvious correlation between KI values and Si content. This indicates the occurrence of other substitutions in addition to the celadonitic one, probably the di–trioctahedral substitution discussed above.

Compositions of chlorite are normalized to 28 oxygens (Table 7) and fulfil the criterion of non-contamination, $\Sigma Ca + Na + K < 0{\cdot}2$ (Dalla Torre *et al.*, 1996*b*). Using the classification of Zane & Weiss (1998), chlorites in the studied samples are trioctahedral type I where ($X_{Mg} + X_{Fe} \geq X_{Al} + X_{vacancy}$). A Fe–Mg–Si diagram reveals intermediate compositions between chamosite and clinochlore (Fig. 8a). X_{Mg} varies between 0·431 and 0·955, and according to Hey (1954), the chlorites lie mainly in the ripidolite, pichnochlore and brunsvigite fields.

The low total interlayer charge of the chlorites ($<0{\cdot}2$ p.f.u.) indicates that smectite or illite impurities are insignificant (Fig. 8b). The increase of (Al^{VI}–Al^{IV}) could be attributed to increasing sudoitic substitution (di–trioctahedral) (Árkai *et al.*, 2003). Correlations observed for apparent octahedral vacancies with (Al^{VI}–Al^{IV}) (Fig. 8c) and apparent octahedral vacancies with sum of octahedral divalent cations (Fig. 8d) prove the sudoitic substitution in the analyzed chlorites. Figure 8e demonstrates that, in addition to the Tschermak substitution, the di–trioctahedral substitution plays an important role in chlorites.

Using the chlorite–Al^{IV} thermometer of Cathelineau (1988), we calculated mean T values between 270 and

Table 5: Correlation between KI, illite–muscovite polytypes transformations, vitrinite reflectance, temperature and mineral parageneses

Metapelitic Zone	KI ($\Delta°2\Theta$)	Polytypes %2M$_1$	Vitrinite Reflectance R$_{max}$ %	T°C	Index Minerals						
					Kln	Corr	C/S	Pg	Lws	Fe-Gln	Mg-Car
Diagenetic Zone	1.74	37.5									
- - - - - - - - - -	*0.42*	- - - - - - - - - -	*2.9 ± 0.2*	*230 ± 10*							
Low Anchizone											
- - - - - - - - - -	*0.30*	100.0	*3.4 ± 0.2*	*260 ± 10*							
High Anchizone											
- - - - - - - - - -	*0.25*	- - - - - - - - - -	*4.8 ± 0.7*	*295 ± 10*							
Epizone											
	0.15			350							

Vitrinite reflectance is after Diessel *et al*. (1978); oxygen isotopic thermometry is after Black (1974); mineral abbreviations are after Kretz (1983).
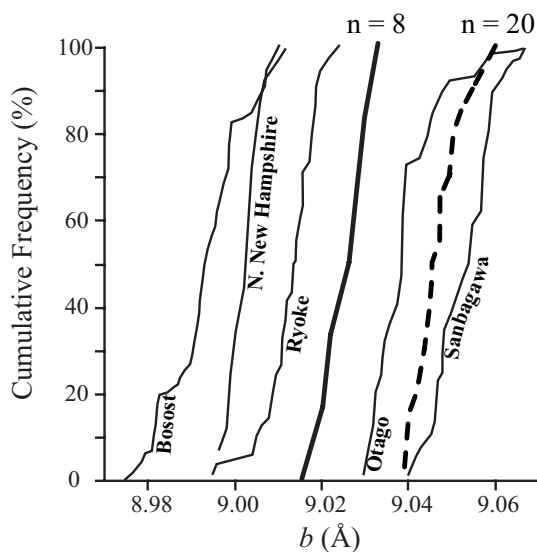
Fig. 6. Cumulative curves of K-white mica *b* cell dimensions for 20 samples from the lawsonite and glaucophane zones (bold dashed line), and eight samples from the pumpellyite–prehnite zone (bold continuous line). Reference curves (fine lines) are from Sassi & Scolari (1974).

340°C (Table 7). Figure 8f shows a negative trend between the metamorphic grade increases (KI values decrease) and the calculated *T*. This could be explained by the absence of smectite contamination (or other significant impurity) (Schmidt *et al.*, 1997).

Index mineral chemistry

Lawsonite is very common in shales from the eastern coast. Representative analyses are presented in Table 8. Petrographic evidence indicates that lawsonite mainly grew during or after development of the main foliation.

Crystals typically are elongated or have undeformed tabular forms in thin section.

Stilpnomelane is relatively widespread in the lawsonite zone, and it is typically associated with lawsonite. Microprobe analyses of the studied stilpnomelane show an X_{Fe} range from 0·70 to 0·80 corresponding to ferro-stilpnomelane (Table 8).

Sodic amphiboles in the Diahot terrane occur as fine-grained, thin, needle-like ellipsoidal fibres parallel to the main foliation, with pale blue to purple pleochroism. Representative analyses of sodic amphibole from samples MF3031 and PS131 are presented in Table 8. The amphiboles are ferro-glaucophane with X_{Mg} ranging between 0·30 and 0·48 (after Leake *et al.*, 1997).

Vein mineralogy, textural relationships and microthermometry

We selected quartz-vein samples from four localities along the profile between Koumac and Ouégoa (Fig. 3). Oriented samples were collected from structurally controlled syntectonic fissures of a few millimetres in width. Rock sections were cut perpendicular to the bedding and retaining portions of the wall-rock. The chronology of the different fluid inclusion populations (Table 9) is defined with respect to their relative overgrowth sequence (Mullis, 1976).

Veins are mainly composed of small quartz crystals, except sample MF3006, which contains, in addition, calcite and chlorite. Two types of fluid inclusions were identified with the microscope: one-phase inclusions and two-phase fluid inclusions (consisting of vapour and liquid at room temperature). Most of the fluid inclusions analyzed are secondary.

Table 6: Representative chemical analyses of K-white micas

Sample no.:	MF3031		MF3144		MF3003		PS22(1)		PS22(2)		PS32		PS89		PS54		PS56	
n:	15	SD	11	SD	6	SD	19	SD	4	SD	14	SD	8	SD	21	SD	17	SD
SiO_2	50·10	0·69	50·72	0·84	45·50	0·96	52·38	0·87	48·91	1·30	51·96	0·74	47·60	1·61	50·01	1·46	49·69	0·72
TiO_2	0·10	0·12	0·09	0·07	0·25	0·19	0·08	0·08	0·15	0·22	0·07	0·07	0·10	0·16	0·06	0·05	0·04	0·06
Al_2O_3	26·56	0·75	24·42	0·47	35·36	0·77	24·04	0·68	28·94	2·01	24·31	0·87	33·25	2·84	23·61	2·08	24·54	1·03
FeO	3·87	0·35	4·49	0·67	1·75	1·03	4·37	0·42	5·39	1·71	4·50	0·57	1·25	1·65	2·79	0·80	4·83	0·66
MnO	0·12	0·06	0·03	0·03	0·03	0·03	0·03	0·04	0·02	0·03	0·11	0·07	0·03	0·04	0·05	0·06	0·07	0·05
MgO	2·64	0·08	3·34	0·12	0·78	0·32	3·69	0·29	2·30	0·66	3·14	0·41	2·04	0·73	4·37	0·81	2·82	0·49
CaO	0·02	0·03	0·05	0·06	0·02	0·02	0·05	0·05	0·03	0·02	0·04	0·05	0·01	0·01	0·02	0·03	0·04	0·03
Na_2O	0·29	0·07	0·09	0·03	0·73	0·27	0·24	0·24	0·20	0·21	0·10	0·05	0·88	0·44	0·08	0·09	0·11	0·07
K_2O	10·45	0·44	9·37	0·31	9·58	0·84	10·88	0·31	10·34	1·06	10·94	0·21	9·49	0·96	10·41	0·39	10·78	0·26
Total	94·16	0·99	92·60	0·40	94·19	1·13	95·77	0·71	96·28	0·24	95·17	0·69	94·62	1·35	91·41	0·69	92·92	0·64
Si	3·41	0·03	3·50	0·03	3·06	0·03	3·52	0·03	3·28	0·08	3·51	0·03	3·17	0·08	3·49	0·09	3·46	0·05
Ti	0·01	0·00	0·00	0·00	0·01	0·01	0·00	0·00	0·01	0·01	0·00	0·00	0·00	0·01	0·00	0·00	0·00	0·00
Al^{IV}	0·59	0·03	0·50	0·03	0·94	0·03	0·48	0·03	0·72	0·08	0·49	0·03	0·83	0·08	0·51	0·09	0·54	0·05
Al^{VI}	1·54	0·02	1·48	0·03	1·87	0·05	1·42	0·03	1·57	0·08	1·45	0·04	1·78	0·13	1·44	0·10	1·47	0·04
Fe^{2+}	0·22	0·02	0·26	0·04	0·10	0·06	0·25	0·02	0·30	0·10	0·25	0·03	0·07	0·10	0·16	0·05	0·28	0·04
Mn	0·01	0·00	0·00	0·00	0·00	0·00	0·00	0·00	0·00	0·00	0·01	0·00	0·00	0·00	0·00	0·00	0·00	0·00
Mg	0·27	0·01	0·34	0·01	0·08	0·03	0·37	0·03	0·23	0·27	0·32	0·04	0·20	0·08	0·46	0·09	0·29	0·05
Ca	0·00	0·00	0·00	0·00	0·00	0·00	0·00	0·00	0·00	0·00	0·00	0·00	0·00	0·00	0·00	0·00	0·00	0·00
Na	0·04	0·01	0·01	0·00	0·09	0·03	0·03	0·03	0·03	0·03	0·01	0·01	0·11	0·06	0·01	0·01	0·01	0·01
K	0·91	0·04	0·82	0·03	0·82	0·07	0·93	0·03	0·88	0·09	0·94	0·02	0·81	0·10	0·93	0·04	0·96	0·02
t.i.c.	0·95	0·03	0·83	0·03	0·91	0·05	0·96	0·02	0·91	0·11	0·95	0·02	0·92	0·06	0·94	0·03	0·97	0·02
b_0	9·04		9·05		9·01		9·05		9·04		9·05		9·02		9·05		9·05	
KI	0·17		0·14		0·35		0·17		—		0·18		—		0·19		0·20	

Calculations are based on 11 oxygens (anhydrous basis). b_0 values calculated after Guidotti *et al*. (1989). (1) Syn-kinematic K-white micas; (2) post-kinematic K-white micas. SD, standard deviation; *n*, number of samples; t.i.c., total interlayer cations (Ca + Na + K).

Different fluid inclusion assemblages can be defined (Table 9) based on their shape, salinity and relation to each other. We generally observed a first fluid inclusion assemblage stretched, partially or totally decrepitated (fluid inclusion assemblage 1). Fluid inclusions, with a high volatile ratio (≥80%) and well shaped (negative quartz), are present in samples MF3022 and MF3027. Such fluid inclusions were formed during a heating event, postdating the deformation. In the case of sample MF3027, it was not possible to measure Th_I because of the variation of the vapor/liquid ratios after repeated measurement. Fluid inclusions less stretched, with lower salinity, were observed in samples MF3004 and MF3027 and define a third fluid assemblage in those samples.

P–T estimates: equilibrium phase diagrams

Sample MF3031 is from the lawsonite–glaucophane zone of the Diahot terrane, in the district of Ouégoa. Sample MF2994 was collected in the pumpellyite–prehnite zone (high diagenetic to low anchizone) of the Koumac terrane. Equilibrium phase diagrams were calculated using the THERIAK-DOMINO software. The main input consists of the modal bulk composition of the rock. To attain greater control on the model, bulk compositions without the minor elements were calculated in the systems NKFMASH (MF2994, where Ca and Ti are in minor amounts) and Ti–Ca–NKFMASH (MF3031). Calculations were performed in the temperature range between 150 and 500°C and for pressures between 0·1 and 2·0 GPa. We took also into account the effect of water activity on the stability of mineral assemblages. The water activity was evaluated to 0·9 for sample MF3031 on the basis of a previous study on the mineral and bulk-rock oxygen and carbon isotopic characteristics of the Ouégoa terrane (Black, 1977).

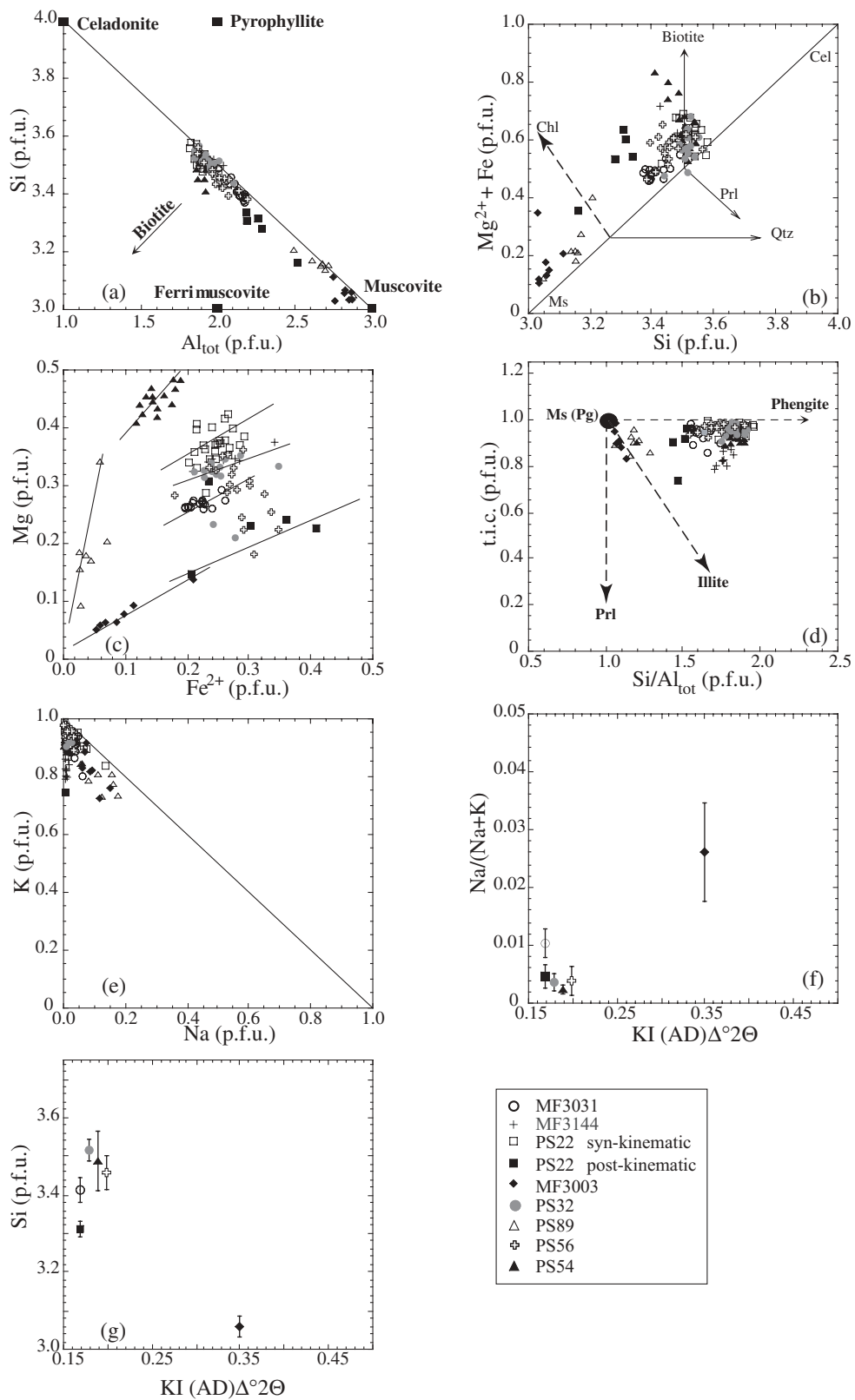The *P–T* section for sample MF3031 (Fig. 9) shows the observed mineral assemblage of the sample

Fig. 7. (a–e) Compositional relations of metamorphic dioctahedral white micas. Cation numbers and ratios are calculated from electron microprobe analyses. t.i.c., total interchange charge = K + Na + 2Ca per formula unit. (f, g) Relations between illite crystallinity (KI) and the chemistry of white mica.

Table 7: Representative chemical analyses of chlorite

Sample no.:	MF3144		MF3155*		MF3023*		PS22		PS32		PS89		PS131	
n:	6	SD	11	SD	15	SD	12	SD	7	SD	5	SD	4	SD
SiO_2	25·48	0·39	27·86	0·70	30·42	0·44	26·65	0·50	26·01	0·66	28·19	0·89	24·93	0·31
TiO_2	0·08	0·07	0·01	0·02	0·03	0·04	0·03	0·02	0·03	0·03	0·00	0·09	0·03	0·04
Al_2O_3	17·19	0·33	17·95	0·52	16·52	0·26	18·82	0·47	18·75	0·54	23·65	0·68	20·25	0·14
FeO	32·12	0·58	26·04	0·79	12·58	0·63	30·52	0·58	32·82	0·35	14·38	0·64	29·15	0·38
MnO	0·45	0·04	0·31	0·06	0·14	0·03	0·28	0·09	0·43	0·08	0·14	0·07	0·72	0·10
MgO	10·72	0·11	15·54	0·47	25·71	0·58	11·75	0·19	9·76	0·15	20·74	0·18	10·88	0·24
CaO	0·02	0·02	0·25	0·12	0·15	0·04	0·02	0·04	0·03	0·03	0·00	0·01	0·09	0·04
Na_2O	0·02	0·02	0·01	0·02	0·03	0·02	0·05	0·08	0·04	0·02	0·03	0·02	0·02	0·01
K_2O	0·07	0·07	0·03	0·02	0·02	0·02	0·03	0·02	0·03	0·03	0·23	0·18	0·04	0·01
Total	86·14	0·57	88·00	0·45	85·60	0·84	88·14	0·65	87·90	1·15	87·41	1·06	86·09	0·50
Si	5·72	0·04	5·87	0·12	6·12	0·08	5·74	0·09	5·70	0·09	5·58	0·11	5·49	0·03
Ti	0·01	0·01	0·00	0·00	0·00	0·01	0·01	0·01	0·00	0·00	0·00	0·01	0·00	0·01
Al^{IV}	2·28	0·04	2·13	0·12	1·88	0·08	2·26	0·09	2·30	0·09	2·42	0·11	2·51	0·03
Al^{VI}	2·27	0·09	2·32	0·07	2·03	0·05	2·52	0·07	2·55	0·06	3·09	0·13	2·75	0·03
Fe^{2+}	6·03	0·13	4·59	0·16	2·11	0·10	5·50	0·11	6·02	0·06	2·38	0·13	5·37	0·08
Mn	0·01	0·01	0·06	0·01	0·02	0·00	0·05	0·02	0·08	0·01	0·02	0·01	0·13	0·02
Mg	3·59	0·05	4·88	0·14	7·71	0·14	3·77	0·06	3·19	0·04	6·12	0·14	3·57	0·07
Ca	0·01	0·01	0·06	0·03	0·03	0·01	0·01	0·01	0·01	0·01	0·00	0·00	0·02	0·01
Na	0·01	0·01	0·01	0·01	0·01	0·01	0·02	0·03	0·02	0·01	0·01	0·01	0·01	0·01
K	0·02	0·01	0·01	0·01	0·01	0·01	0·01	0·01	0·01	0·01	0·06	0·05	0·01	0·00
$Fe^{2+}/(Fe^{2+} + Mg)$	0·63	0·00	0·48	0·01	0·21	0·01	0·59	0·01	0·65	0·00	0·28	0·01	0·60	0·01
$T°C$	305	7	281	19	241	12	302	14	312	9	328	17	341	5

Calculations are based on 28 oxygens (anhydrous basis). *n*, number of samples; SD, standard deviation. All Fe is assumed to be Fe^{2+}. Temperatures are determined using the chlorite thermometer of Cathelineau (1988).
*Samples MF3155 and MF3023 are metabasites; others are pelites.

(quartz + phengite + glaucophane + chlorite + lawsonite + titanite). The assemblage is stable over a wide range of *P* and *T*, going from 0·8 to 1·8 GPa and from 300 to 475°C. To gain a better constraint, we calculated the isopleths of Fe-Gln and Ms (Fig. 9). These mineral compositions allow us to restrict the stability field to 1·3–1·8 GPa and 400–475°C. The *b* cell dimension of samples in the zone, 9·04 Å, reflects the highipressure character of metamorphism and points to pressure higher than 1·2 GPa in the temperature range of 400–475°C using the *P–T* diagram of Ramírez & Sassi (2001, Fig. 9).

Calculations for sample MF2994 from the pumpellyite–prehnite zone (high diagenetic to low anchizone) required accurate evaluation of the a_{H_2O}. Black (1977) has shown that in this zone, a_{H_2O} ranges between 0·6 and 0·7. Calculations determined for a maximum a_{H_2O} of 0·7 [value for maximum a_{H_2O} of Black (1977)] show a maximum temperature of 250°C for a pressure of 0·3 GPa for the assemblage Qtz + K-white mica + Kln + Chl (observed in sample MF2994) (Fig. 10). Therefore,

we can postulate *P–T* conditions below 250°C and 0·3 GPa in the very low-grade region, which is consistent with estimates by Bell & Brothers (1985) based on the appearance at a slightly higher grade of lawsonite and aragonite in the lawsonite zone.

DISCUSSION
Comparison of methods to determine the HP–LT event ('peak metamorphism')

In the NE of New Caledonia, in the Oligocene HP–LT schist belt, the trends shown by KI values can be reproduced from the vitrinite reflectance measurements published by Diessel *et al.* (1978). Vitrinite reflectance data show an evolution from medium-volatile bituminite to meta-anthracite stage (1·4–6·5% R_{max}). In the HP epizone of the lawsonite–glaucophane zone, the maturation of vitrinite reaches the optical graphite stage. In Table 5, the high diagenesis and low anchizone (semi-anthracite
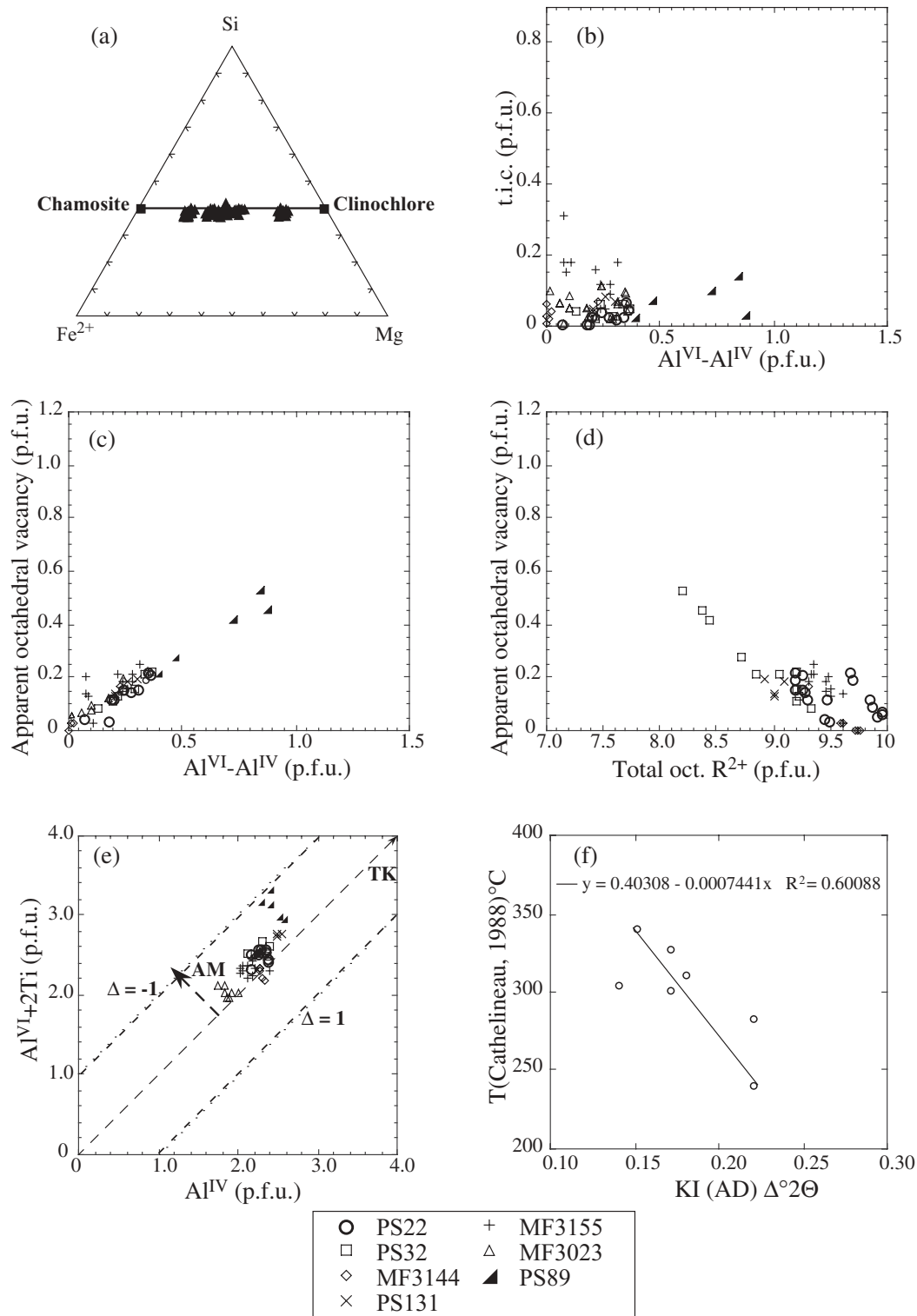
Fig. 8. (a–e) Compositional variation of chlorite. Cation numbers and ratios are calculated from electron microprobe analyses. (a) Fe^{2+}–Mg–Si diagram for chlorites that plot close to a straight line between the end-members chamosite and clinochlore. (b) t.i.c. (total interchange charge = K + Na + 2Ca per formula unit) vs Al^{VI}–Al^{IV}. (c) Apparent octahedral vacancy (= 20 − Σoctahedral cations per formula unit) vs Al^{VI}–Al^{IV}. (d) Apparent octahedral vacancy vs total octahedral R^{2+} (= Fe^{2+} + Mg^{2+}). (e) Al^{VI} + 2Ti vs Al^{IV}. Arrows show trends of TK (Tschermak) and AM (dioctahedral) substitutions, where $\Delta = Al^{IV} − (Al^{VI} + 2Ti)$. (f) Correlation between peak temperature of metamorphism calculated with the Cathelineau (1988) thermometer and KI values.

Table 8: Representative chemical analyses of Fe-stilpnomelane (Fe-Stp), lawsonite (Lws), Fe-glaucophane (Fe-Gln) and Mg-carpholite (Mg-Carph)

Mineral:	Fe-Gln		Fe-Gln		Lws		Lws		Lws		MgCarph		Fe-Stp		Fe-Stp		Fe-Stp	
Sample no.:	MF3031		PS131		MF3031		PS131		MF3144		PS89		MF3144		PS32		PS22	
n:	23	SD	6	SD	4	SD	4	SD	15	SD	15	SD	19	SD	9	SD	7	SD
SiO_2	54·51	1·28	55·63	0·64	37·74	0·96	37·70	1·06	38·93	1·50	38·64	0·78	45·25	1·47	45·18	1·61	46·92	0·85
TiO_2	0·09	0·08	0·11	0·08	0·17	0·17	0·23	0·18	0·11	0·14	0·18	0·16	0·04	0·05	0·07	0·07	0·10	0·11
Al_2O_3	10·24	0·51	11·98	0·29	31·45	1·46	32·03	0·42	28·99	1·33	32·84	0·54	6·14	0·52	6·57	0·40	6·59	0·41
FeO	18·45	1·01	16·21	0·28	0·44	0·05	0·40	0·09	0·37	0·17	6·45	0·62	28·62	0·83	29·41	0·84	27·45	1·64
MnO	0·38	0·13	0·29	0·12	0·04	0·04	0·03	0·03	0·04	0·04	0·12	0·08	1·17	0·09	1·10	0·11	0·62	0·06
MgO	4·48	0·24	5·55	0·16	0·01	0·01	0·02	0·02	0·05	0·07	9·16	0·39	5·19	0·34	4·85	0·26	6·62	0·31
CaO	0·41	0·18	0·32	0·17	16·92	0·30	16·79	0·30	16·39	0·55	0·01	0·01	0·03	0·02	0·03	0·02	0·12	0·08
Na_2O	6·74	0·19	7·13	0·07	0·02	0·01	0·03	0·01	0·26	0·10	0·02	0·01	0·31	0·34	0·23	0·13	0·26	0·34
K_2O	0·09	0·17	0·02	0·02	0·05	0·04	0·07	0·08	0·09	0·13	0·03	0·04	4·30	1·37	3·47	1·35	2·54	1·48
Total	95·39	0·71	97·24	0·48	86·92	2·09	87·28	1·04	85·04	1·55	87·44	0·63	91·06	0·95	90·90	0·72	91·21	1·53
Si	7·95	0·14	7·87	0·05	2·02	0·03	2·00	0·04	2·13	0·07	2·00	0·03	8·00	—	8·00	—	8·00	—
Ti	0·01	0·01	0·01	0·01	0·01	0·01	0·01	0·01	0·00	0·01	0·01	0·01	0·01	0·01	0·01	0·01	0·01	0·01
Al_{tot}	1·76	0·09	2·00	0·05	1·98	0·04	2·01	0·03	1·87	0·06	2·00	0·03	1·28	0·11	1·37	0·11	1·33	0·09
Al^{IV}	0·11	0·05	0·13	0·05	—	—	—	—	—	—	—	—	—	—	—	—	—	—
Al^{VI}	1·68	0·09	1·87	0·03	—	—	—	—	—	—	—	—	—	—	—	—	—	—
Fe^{3+}	0·31	0·10	0·19	0·03	—	—	—	—	—	—	—	—	—	—	—	—	—	—
Fe^{2+}	1·97	0·08	1·73	0·03	0·02	0·00	0·02	0·00	0·02	0·01	0·28	0·03	4·24	0·20	4·36	0·20	3·91	0·21
Mn	0·05	0·02	0·04	0·01	0·00	0·00	0·00	0·00	0·00	0·00	0·01	0·00	0·18	0·01	0·17	0·02	0·09	0·01
Mg	0·97	0·05	1·17	0·03	0·00	0·00	0·00	0·00	0·00	0·01	0·71	0·03	1·37	0·11	1·28	0·10	1·68	0·08
Ca	0·06	0·03	0·05	0·03	0·97	0·02	0·96	0·02	0·96	0·04	0·00	0·00	0·01	0·00	0·01	0·00	0·02	0·02
Na	1·91	0·06	1·96	0·02	0·00	0·00	0·00	0·00	0·01	0·01	0·00	0·00	0·11	0·11	0·08	0·04	0·09	0·11
K	0·02	0·03	0·00	0·00	0·00	0·00	0·00	0·01	0·01	0·01	0·00	0·00	0·98	0·34	0·79	0·32	0·55	0·32
Fe/(Fe + Mg)	0·70	0·02	0·62	0·01	—	—	—	—	—	—	0·28	0·03	0·77	0·02	0·76	0·02	0·75	0·02

Calculations are based on eight Si for Fe-Stp, five cations for Lws, 23 oxygens for Fe-Gln and eight oxygens for Mg-Carph (for simplification an anhydrous basis is used for amphibole and carpholite). *n*, number of samples; SD, standard deviation.

stage) correlates with the appearance of $1 M_d$ mica, kaolinite, corrensite and pumpellyite. The high anchizone (anthracite stage) correlates with the occurrence of $2 M_1$ mica, lawsonite, chlorite–smectite and pumpellyite. The epizone (high meta-anthracite stage, including the incipient semi-graphite to optical graphite stage) correlates with the stability field of chlorite, lawsonite, glaucophane and carpholite. The evolution of sheet silicates coherently reflects the coalification trend and the field gradient of increasing HP metamorphism.

In New Caledonia, R_{max} values (Diessel *et al.*, 1978) for the KI anchizone boundaries are $2·95 \pm 0·15\%$ (high diagenetic zone–low anchizone), and $4·75 \pm 0·7\%$ (high anchizone–epizone). In other metamorphic belts, anchizone boundaries, in terms of vitrinite reflectance, were set to be 2·5–3·1% and 3·7–5·5% with a mean R_0 [$R_0 = (2R_{max} + R_{min})/3$] for the lower and upper limit of the

anchizone, respectively (Kisch, 1987). A wider range of $R_{max}\%$ values was subsequently recognized in different tectonic nappes of the Alps and in a literature revision by Ferreiro Mählmann (1994). More restricted ranges have been proposed by Underwood *et al.* (1991), but those workers did not take into account reaction kinetics of processes such as illitization and coalification, which are strongly controlled by the tectono-thermal and heat flow history (Frey *et al.*, 1980; Ferreiro Mählmann, 2001). A recent study by Ernst & Ferreiro Mählmann (2004) has shown that oxygen fugacity and water activity have no influence on vitrinite reflectance. Thus, the following discussion is focused on the thermal history and geodynamic evolution.

Using the minimum pressure limit (1·2 GPa), deduced from the *b* cell dimension method for the low epizone (300°C, lawsonite zone), in the maturity kinetics model of

Table 9: Fluid inclusion microthermometric data

1	2	3	4	5	6	7	8	9	10	11	12	13	14
Locality	FP	HM	IT	n_l	D/RI	V%	T_e	Tm_{ICE}	Th_l	CH_4 (mol %)	CO_2 (mol %)	H_2O (mol %)	NaCl (mol %)
MF3004	1	FQ	Ps II	26	str., part. decrep., re-equilibr.	5	−54	−0·8; ms	138/131, 148	n.d.	n.d.	99·6	0·4
MF3004	2	VQ	II	1		0	−75	−23	n.m.	n.d.	n.d.	91·6	8·4
MF3004	3	VQ	II	3		6	−56	−0·8; ms	151/149, 154	n.d.	n.d.	99·6	0·4
MF3006	1	VQ	II	12	LFI decrep., SFI str., re-equilibr.	∼4	−53	−1·5; ms	127/117, 135	n.d.	n.d.	99·2	0·8
MF3022	1	VQ	II	13	LFI decrep., SFI str., re-equilibr.	∼4	−61	−2·1, −2·2, −2·0; ms	122/117, 130	n.d.	n.d.	98·9	1·1
MF3022	2	VQ	II	11		10−≥80	n.m.	−2·7, −3·2, −2·0; ms	165−404	n.d.	n.d.	98·6	1·4
MF3027	1	VQ	II	2	LFI decrep.	∼10	−55	−2·5, −2·6, −2·5; ms	n.m.	n.d.	n.d.	98·7	1·3
MF3027	2	VQ	II	6		≥90	n.o.		n.o.	n.d.	n.d.	n.o.	n.o.
MF3027	3	VQ	II	14		∼4	−60	−0·9, −1·0, −0·8	121/112, 129	n.d.	n.d.	99·5	0·5

1, Locality number of Martin Frey. 2, FP, fluid inclusion population. 3, HM, host mineral. (FQ, fibre quartz; VQ, vein quartz.) 4, IT, inclusion type. (Ps II, pseudosecondary fluid inclusions; II, secondary fluid inclusions.) 5, n_l, number of measured fluid inclusions. 6, D/RI, deformation and re-equilibration of fluid inclusions. (str., stretched; part. decrep., partially decrepitated; decrep., decrepitated; re-equilibr., re-equilibrated; LFI, large fluid inclusions; SFI, small fluid inclusions.) 7, V%, volume per cent of the volatile part estimated at room temperature. 8, T_e, eutectic temperature of fluid inclusions (°C). 9, Tm_{Ice}, melting temperature of ice (°C). (First number is mean value; second and third numbers are extreme values; ms; metastable.) 10, Th_l, homogenization temperature of fluid inclusions. (First number is mean value; second and third numbers are extreme values.) 11−14, approximate mole per cent of CH_4, CO_2, H_2O and NaCl (equivalents). n.d., not detected; n.o., not observed; n.m., not measured.

Dalla Torre *et al.* (1997), which predicts that pressure lowers vitrinite reflectance, we tried to reproduce the measured maturity (VR) of 5·0–5·5% R_{max}. The low epizone with an HP metamorphic facies was chosen, because at higher temperatures, diagnostic use of KI and vitrinite reflectance is not recommended (Ferreiro Mählmann, 1994, 2001). Dependent on the time factor, the modeled vitrinite reflectance value is 2·8% R_{max} for 1 Ma and 3·4% R_{max} for 12 Ma. The maximum time range of 12 Ma is limited by sediment ages (Early Eocene) and cooling ages (Late Eocene; see Ghent *et al.*, 1994). Hence, using the thermo-barometric model of vitrinite reflectance of Dalla Torre *et al.* (1997), it is not possible to reproduce the vitrinite reflectance observed in New Caledonia.

Our modeling shows that the KI–VR mineral zone relationship was probably not established during maximum pressure metamorphism. The field of equilibrium between the different parameters that were used to determine metamorphic grade was probably reached in a later stage during retrogression. Fluid inclusions cannot be used to restore 'peak conditions' of the HP–LT metamorphism because the first population is decrepitated. It is evident that parameters such as vitrinite reflectance, illite crystallinity, fluid inclusion data, mica *b* cell dimension data and mineral zoning define different points on a *P–T* path.

Pressure–temperature path evolution

Bell & Brothers (1985) demonstrated an increase of temperature during exhumation in the lawsonite zone. This *P–T* path was constrained by the transformation of lawsonite to zoisite (Lws + Ab ⇔ Zo + Pg + Qtz + vapor). The reaction is controlled by the instability of lawsonite in the presence of CO_2 generated by concurrent decarbonation, associated with conditions favorable for oxidation of Fe and growth of epidote. At the transition between lawsonite and epidote–blueschist zone, all organic matter changed to an increasingly ordered graphite structure (Diessel *et al.*, 1978). The concomitant appearance of optical graphite and epidote suggests that heat generated by decarbonation reactions may have enhanced the ordering of carbon in graphite, even though the pressure at that time was decreasing (Bell & Brothers, 1985). In the same way, Yokoyama *et al.* (1986) presented, in the higher metamorphic zones, a *P–T* path including a temperature-prograde phase of climax crystallization that prevailed during a decline in pressure.
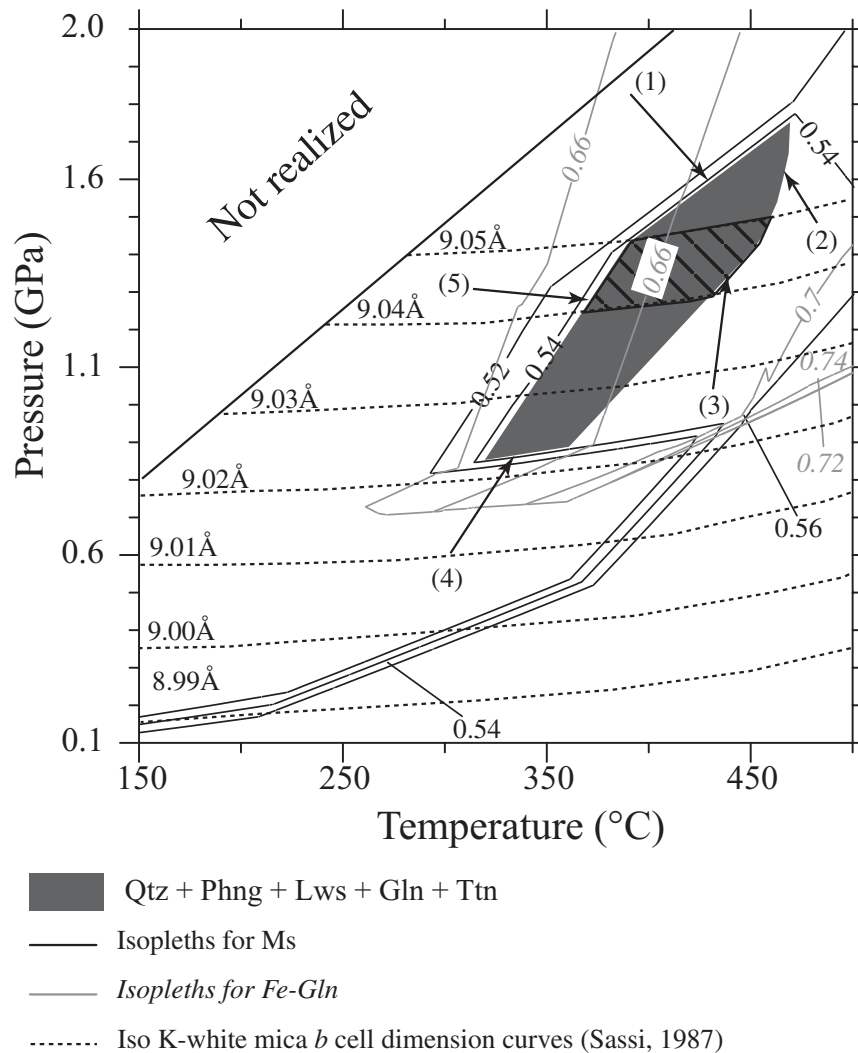
Fig. 9. Pressure–temperature conditions for sample MF3031 (glaucophane zone near Ouégoa) using the thermodynamic software THERIAK-DOMINO. The stability field of the mineral parageneses found in this sample is represented in dark grey. Reactions at the boundary of the stability field are labelled as follows: (1) Qtz + Phng + Lws + Gln + Chl + Ttn = Qtz + Phng + Lws + Gln + Chl + Ttn + Rt; (2) Qtz + Phng + Lws + Gln + Chl + Ttn = Qtz + Phng + Gln + Grt + Chl + Ttn; (3) Qtz + Phng + Lws + Gln + Chl + Ttn = Qtz + Phng + Zo + Gln + Chl + Ttn; (4) Qtz + Phng + Lws + Gln + Chl + Ttn = Qtz + Phng + Lws + Gln + Chl + Ab + Ttn; (5) Qtz + Phng + Lws + Gln + Chl + Ttn = Qtz + Phng + Lws + Pg + Gln + Chl + Ttn. Iso W-white mica *b* cell dimension curves (dashed lines) are from Ramírez & Sassi (2001). The diagonally shaded area corresponds to the K-white mica *b* cell dimension values measured. Isopleths for Ms and Fe-Gln were computed with THERIAK-DOMINO.

During or after decompression, an increase of temperature is also indicated by the maturity of organic matter, which is higher than expected in a blueschist-facies metamorphic environment (Dalla Torre *et al.*, 1997). We tried to reproduce the evolution of organic matter in New Caledonia using three kinetic models. An increase in temperature and heat flow is the easiest way to elevate vitrinite reflectance in kinetic maturity models (Model 1). Hence, using the kinetic maturity model from Dalla Torre *et al.* (1997), but lowering the pressure conditions, it is also possible to increase the modeled vitrinite reflectance values to the measured values of 5·0–5·5% R_{max} with a small increase of the temperature. At 0·4 GPa and 350°C, the best fit is attained for a model in which the maximum temperature is attained at 1 Ma, corresponding to a vitrinite reflectance of 4·9% R_{max}; at 12 Ma the vitrinite reflectance increases to 5·8% R_{max} (outside the calibrated range of the model). Following these observations, a Model 2 could be proposed. If cooling occurred at higher pressures, a long period of heating and slow decompression is required to inhibit or prevent suppression of vitrinite reflectance. If decompression was fast and heating took place mainly at much lower pressures, a short time span of heating is preferable (pressure retardation can be neglected). This last model, Model 3, is supported by the significant Si decrease from the
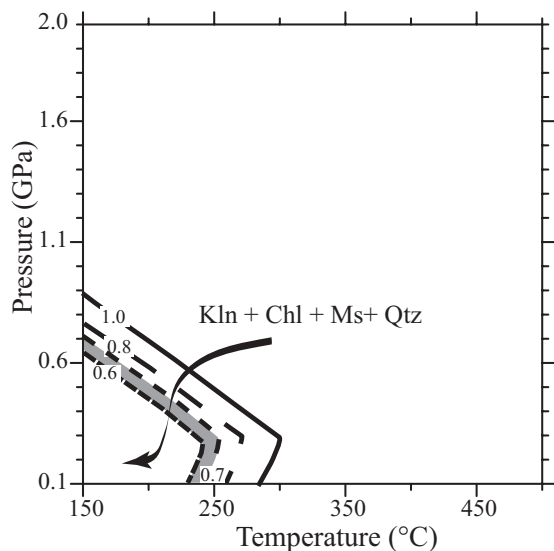
Fig. 10. Different pressure–temperature stability ranges for the assemblage Kln–Chl–Ms–Qtz calculated for different values of water activity (from 0·6 to 1·0).

syn-kinematic mica (3·52 a.pf.u.) to the post-kinematic mica (3·28 a.p.f.u.) (Fig. 7a). In that case, the HP minerals are pre- to syn-kinematic with respect to the ductile deformation (main foliation). The decrease of the celadonite content points to a decrease of pressure (Ernst, 1963; Massonne & Szpurka, 1997) after the main deformation.

Support for an isothermal uplift model is provided by the first fluid inclusion assemblage, where the fluid inclusions are stretched (in the SW) or decrepitated (towards the NE). Once entrapped and enclosed, the pressure in any fluid inclusion is defined by the isochore valid for the fluid density and composition at the time of trapping. In the case of isothermal uplift, fluid inclusions have higher pressure than the ambient pressure. The inclusion can expand or lose a part of its content by leakage through microfissures and dislocations. This process is referred to as 'explosion-decrepitation' (Van den Kerkhof & Hein, 2001).

The second fluid inclusion assemblage is water-rich. In general, the Th_I values cluster around 150°C and are similar at all locations irrespective of the orientation of the vein. In samples MF3022 and MF3027, fluid inclusions of heterogeneous vapor/liquid ratios (up to $\geq 0\cdot 9$) and density are observed. Such fluid inclusions with small bulk densities are common for epithermal events (= boiling event) (Hedenquist, 1991; Valori et al., 1992). The age of this boiling event will postdate the adiabatic decompression event because the related fluid inclusions do not display any stretching or decrepitation features. No relationship between Th_I and R_{max} in the water-rich fluid inclusions is found. The vitrinite reflectance values, like the illite crystallinity measurements along the investigated cross-section from Koumac to Ouégoa, indicate an

increasing degree of metamorphism from SW to NE. This feature is not observed in the water-rich fluid population.

Maturation of the organic matter in New Caledonia

A comparison of the exhumation path in New Caledonia and in the Diablo Range (California) reveals contrasted trends (Fig. 11). In the Diablo Range, Dalla Torre et al. (1996a) observed a retardation of the maturation of organic matter compared with the KI values, whereas vitrinite reflectance results from New Caledonia are consistent with those found in LP–LT domains in the Central Alps (Ferreiro Mählmann, 1995, 1996) (Fig. 12a and b). The strongest correlation is with those areas where the geodynamic conditions of Barrovian orogenic metamorphism predominate (heat flow 50–70 mW/m^2, thermal gradient 25–35°C/km^2, $T < 400$°C, pressure gradient 0·25–0·35 GPa/km^2, $P < 4$ GPa) and heating occurred over several million years (e.g. Frey et al., 1980; Ferreiro Mählmann, 1994, 2001; Schmidt et al., 1997). This is in contradiction to the HP mineral paragenesis found and the mica b cell dimensions measured. Both HP indicators are the unique petrological remnants of the early collision during the Eocene of the New Caledonian fragment with an intra-oceanic island-arc system and subduction tectonics (e.g. Black & Brothers, 1977; Clarke et al., 1997).

Slight differences in temperature between New Caledonia and the Diablo Range (Fig. 12a) are not enough to explain the wide differences in the evolution of organic matter. However, contrasts exist in the exhumation P–T paths of New Caledonia and the Diablo Range. In the latter, exhumation was along a cold path (Ernst & Banno, 1991) reproducing the prograde P–T trajectory during retrogression. In New Caledonia, the retrogression path was probably adiabatic (or with a slight increase of the temperature) with concomitant decrease of pressure (Fig. 11). Prograde maturation of the organic matter during isothermal decompression appears to be a feasible explanation. In contrast, in the Diablo Range maturity at near maximum temperature was limited to the HP–LT event. The vitrinite reflectance retardation effect by pressure was frozen as a result of subsequent cooling along a cold retrograde P–T path.

Comparison of K-white mica b cell dimensions in New Caledonia and the Franciscan belt, in both cases, reveals values ranging between 9·01 and 9·07 Å, which are indicators of high-pressure conditions (Sassi, 1972). These K-white mica b cell dimensions suggest that they record the high-pressure stage, and not recrystallization along the decompression path or a later event as suggested by the Kübler index and vitrinite reflectance values. It appears that even if the K-white mica becomes increasingly well crystallized as a response to an increase in
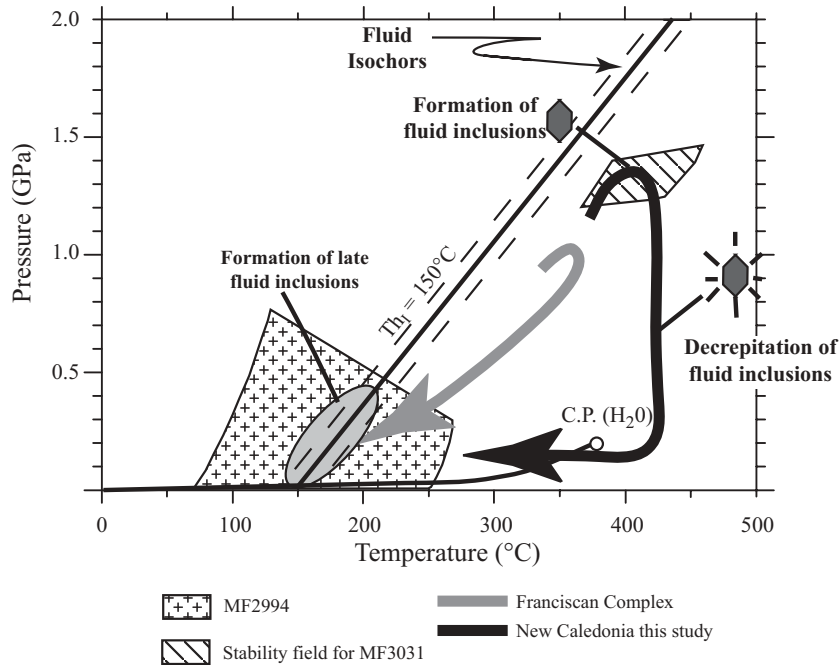
Fig. 11. Sketch of the exhumation path in New Caledonia (black line) compared with that modeled for Pacheo Pass (grey line) by Dalla Torre *et al.* (1996*a*). The stability fields of MF2994 and MF3031 from New Caledonia are indicated. The hexagons schematize fluid inclusions and their evolution along the metamorphic path. The isochor of the two-phase inclusions found systematically in the samples is indicated ($Th_I = 150°C$).
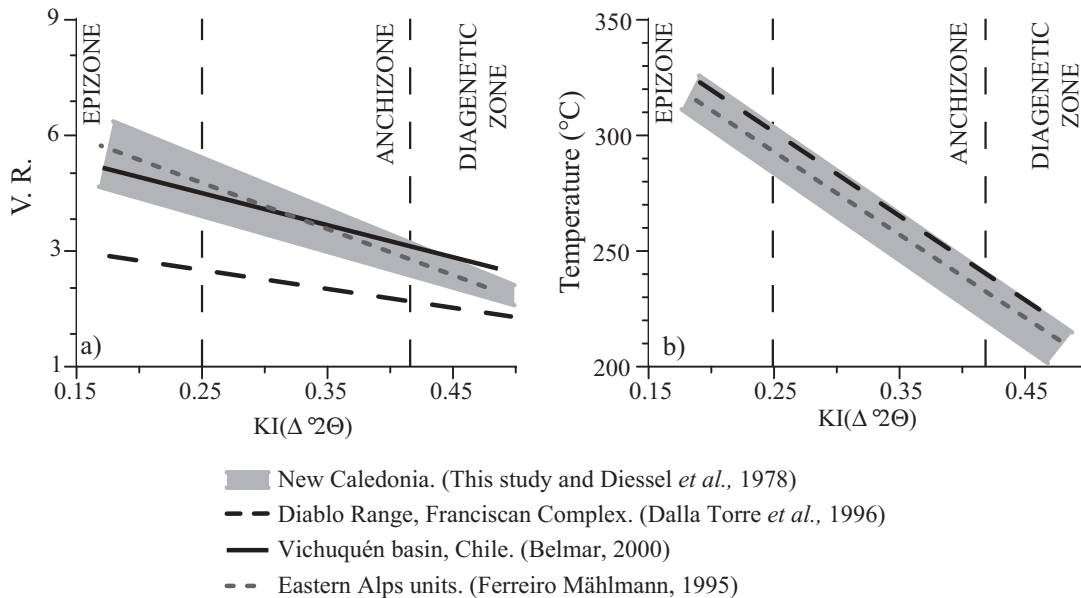

New Caledonia. (This study and Diessel *et al.,* 1978)

– – Diablo Range, Franciscan Complex. (Dalla Torre *et al.,* 1996)

—— Vichuquén basin, Chile. (Belmar, 2000)

- - Eastern Alps units. (Ferreiro Mählmann, 1995)

Fig. 12. Comparisons of New Caledonia data with other metamorphic belts of different pressure and temperature conditions. (a) KI (Kübler index) values vs VR (vitrinite reflectance of % R_{max}) values for New Caledonia, Diablo Range, Vichuquén Basin (Chile) and the Eastern Alps units of Graubünden (Switzerland). (b) KI values vs temperature for New Caledonia, Diablo Range and Eastern Alps units of Graubünden (Switzerland).

temperature, the *b* cell dimension will still preserve the effect of the pressure (no modification of the *b* parameter). This is confirmed by comparing the calculated *P–T* conditions and those determined using the *b* cell dimensions (Sassi, 1987).

As shown above, maturation on an isothermal decompression path can be modeled using different time ranges of heating. The vitrinite reflectance–KI relationship, compared with the metamorphic mineral assemblages, can give another important indicator for the approximate

time span of heating. As described by Teichmüller (1987), because of a higher reaction rate, coalification is more sensitive to the duration of near peak temperature heating than illite crystallinity (Wolf, 1978).

Combining our KI data with the organic matter studies of Diessel *et al.* (1978), the same VR–KI–graphitization trends as described above are found in the same temperature range between 250 and 400°C in the Alps (Ferreiro Mählmann, 2001; Ferreiro Mählmann *et al.*, 2002). These areas in the Alps are defined by low pressures (<0·4 GPa) and a long duration of metamorphic thermal conditions (5–20 Myr) or by greenschist-facies metamorphism overprinting an older blueschist-facies event. A long period of heating during slow exhumation will promote mineral reaction, leading illite to equilibrate with organic material. Long duration of metamorphism at constant temperature, close to steady-state thermal conditions, in an orogenic metamorphic setting (Ferreiro Mählmann, 2001), or during a nearly isothermal exhumation path (this study) will lead to the same KI–VR–*T*°C relationship. Therefore, the relationship described by Ferreiro Mählmann (2001) is probably generally valid for estimating the state of advancement of different reactions at a specific temperature during very low- and low-grade metamorphism. In contrast to the conditions in the Alps (around 20 Myr), the period for reaching equilibrium in New Caledonia (<12 Myr) was much shorter.

Another way to explain the KI–VR–*T*°C correlation would be to document the effect of tectonic strain on illite crystallinity. As illustrated by Merriman *et al.* (1995), tectonic strain can promote dislocations and subgrain development (i.e. a decrease in KI) as stored elastic strain promotes dislocation creep. Coalification and graphitization can also be enhanced by strain, resulting in elevated vitrinite reflectance values (Teichmüller, 1987; Árkai *et al.*, 2002; Ferreiro Mählmann *et al.*, 2002). These phenomena are evident in rocks with a tight penetrative foliation and higher amounts of deformation than that observed in our samples. Contrasting trends between mylonitic and less deformed rocks were not detected (Árkai *et al.*, 2002).

CONCLUSIONS

The pre-, syn- and post-metamorphic/kinematic mineral assemblages, K-white mica evolution, fluid inclusion evolution and vitrinite maturity documented in the rocks from New Caledonia are compatible with a model that involves slow isothermal decompression after HP–LT metamorphism. Such *P–T* evolution is probably due to thermal rebound in the upper crust after stacking of nappes during subduction and collision, followed by obduction of the Poya nappe together with the ophiolite

nappe on top of all other units. After transportation to deep crustal levels during initial subduction, and continuous thrusting of the HP nappes on the accretional nappe stack, exhumation in a subduction channel [as described by Chemenda *et al.* (1996)] permitted isothermal decompression. As a result of higher temperatures at greater depth during subduction, the lower viscosity of the rocks allows for fast transportation in the initial stage of exhumation. Later at lower pressure the exhumation slows down (Burov *et al.*, 2001), causing a relaxation of the geotherm. During accretion of the slices, greater heat flow resulted from emplacement of igneous intrusions and kept temperatures elevated. As the rate of exhumation slowed, re-equilibration of organic matter maturation to a typical LT–LP level was achieved. Neither pressure retardation of vitrinite reflectance nor an enhancement of vitrinite reflectance vs Kübler index resulted. Therefore, to reproduce the maturity observed a combination of the three presented models is required. Possibilities include: Model 1, lowering of the pressure of peak metamorphism; Model 2, involving a long period of heating and slow decompression; or Model 3, involving fast decompression and heating at lower pressure. The conditions required for Model 3 best explain the field and petrological observations and the *P–T* evolution from blueschist to greenschist facies. Furthermore, this model is in agreement with the observations of Maurizot *et al.* (1989), and more recently, Fitzherbert *et al.* (2003), for higher-grade metamorphosed pelites in the area. They show that the pelites of the Diahot and Pouébo terranes underwent two metamorphic events: the first a (classic) prograde pressure and temperature event, and the second at decreasing pressure and increasing temperature.

KI values are in good agreement with temperatures generally proposed for the boundaries of the anchizone in metamorphic belts of medium- to low-pressure gradients (Fig. 12b). Correlation between vitrinite reflectance and KI values show a trend similar to that commonly observed in other low-pressure metamorphic belts (Fig. 12a and b). An adiabatic decompression path during exhumation explains the concordance between the evolution of illite crystallinity and coal rank in New Caledonia; hence organic matter matures during decompression, and no effect of pressure on organic matter is preserved (Fig. 11).

This study shows that the evolution of organic matter and illite crystallinity is not only a function of the temperature and pressure gradient or the maximum temperature and pressure reached, but that it also depends on the *P–T* path evolution through time. It is shown that the *b* cell dimension is a good pressure indicator surviving polyphase and prograde temperature overprints and therefore a robust method to determine pressure in LT domains.

ACKNOWLEDGEMENTS

REFERENCES

Aitchison, J. C., Clarke, G. L., Meffre, S. & Cluzel, D. (1995). Eocene arc–continent collision in New Caledonia and implications for regional southwest Pacific tectonic evolution. *Geology* **23**, 161–164.

Árkai, P., Ferreiro Mählmann, R., Suchy, V., Balogh, K., Sykorová, J. & Frey, M. (2002). Possible effects of tectonic strain on phyllosilicates: a case study from the Kandersteg area, Helvetic Domain, Central Alps, Switzerland. *Schweizerische Mineralogische und Petrographische Mitteilungen* **82**, 273–290.

Árkai, P., Faryad, S. W., Vidal, O. & Balogh, K. (2003). Very low-grade metamorphism of sedimentary rocks of the Meliata unit, Western Carpathians, Slovakia: implications of phyllosilicate characteristics. *International Journal of Earth Sciences* **92**, 68–85.

Bell, T. H. & Brothers, R. N. (1985). Development of *P–T* prograde and *P*-retrograde, *T*-prograde isogradic surfaces during blueschist to eclogite regional deformation/metamorphism in New Caledonia, as indicated by progressively developed porphyroblast microstructures. *Journal of Metamorphic Geology* **3**, 59–78.

Belmar, M., 2000. Low-grade metamorphism in Central Chile at 35 °S. *Unpublished PhD thesis*, University of Basel, Switzerland. 189pp.

Berman, R. G. (1988). Internally-consistent thermodynamic data for minerals in the system $Na_2O–K_2O–CaO–MgO–FeO–Fe_2O_3–Al_2O_3–SiO_2–TiO_2–H_2O–CO_2$. *Journal of Petrology* **29**, 445–522.

Black, P. M. (1974). Oxygen isotope study of metamorphic rocks from Ouégoa District, New Caledonia. *Contributions to Mineralogy and Petrology*, **47**, 197–206.

Black, P. M. (1975). Mineralogy of New Caledonia metamorphic rocks. IV. Sheet silicates from Ouégoa district. *Contributions to Mineralogy and Petrology* **49**, 269–284.

Black, P. M. (1977). Regional high-pressure metamorphism in New Caledonia: phase equilibria in the Ouégoa district. *Tectonophysics* **43**, 83–107.

Black, P. M. & Brothers, R. N. (1977). Blueschist ophiolites in the melange zone, northern New Caledonia. *Contributions to Mineralogy and Petrology* **65**, 69–78.

Black, P. M., Maurizot, P., Ghent, E. D. & Stout, M. Z. (1993). Mg–Fe carpholites from aluminous schists in the Diahot region and implications for preservation of high-pressure/low-temperature schists, northern New Caledonia. *Journal of Metamorphic Geology* **11**, 455–460.

Brothers, R. N. (1970). Lawsonite–albite schists from northernmost New Caledonia. *Contributions to Mineralogy and Petrology* **25**, 185–202.

Brothers, R. N. (1974). High-pressure schists in northern New Caledonia. *Contributions to Mineralogy and Petrology* **46**, 109–127.

Brothers, R. N. & Black, M. C., Jr (1973). Tertiary plate tectonics and high-pressure metamorphism in New Caledonia. *Tectonophysics* **17**, 337–358.

Brothers, R. N. & Yokoyama, K. (1982). Comparison of the high-pressure schist belts of New Caledonia and Sanbagawa, Japan. *Contributions to Mineralogy and Petrology* **79**, 219–229.

Burov, E., Jolivet, L., Le Pourhiet, L. & Poliakow, A. (2001). A thermomechanical model of exhumation of HP and UHP metamorphic rocks in Alpine mountain belts. *Tectonophysics* **342**, 113–136.

Carson, C. J., Clarke, G. L. & Powell, R. (2000). Hydration of eclogite, Pam Peninsula, New Caledonia. *Journal of Metamorphic Geology* **18**, 79–90.

Cathelineau, M. (1988). Cation site occupancy in chlorites and illites as a function of temperature. *Clay Minerals* **23**, 471–485.

Chemenda, A. I., Mattauer, M. & Bokun, A. N. (1996). Continental subduction and a mechanism for exhumation of high-pressure metamorphic rocks: new modelling and field data from Oman. *Earth and Planetary Science Letters* **143**, 173–182.

Clarke, G. L., Aitchison, J. C. & Cluzel, D. (1997). Eclogites and blueschists of the Pam Peninsula, NE New Caledonia: a reappraisal. *Journal of Petrology* **38**, 843–876.

Cluzel, D., Aitchison, J., Clarke, G., Meffre, S. & Picard, C. (1994). Point de vue sur l'évolution tectonique et géodynamique de la Nouvelle-Calédonie (Pacifique, France). *Comptes Rendus de l'Académie des Sciences* **319**, 683–690.

Cluzel, D., Aitchison, J. C. & Picard, C. (2001). Tectonic accretion and underplating of mafic terranes in the Late Eocene intraoceanic fore-arc of New Caledonia (Southwest Pacific): geodynamic implications. *Tectonophysics* **340**, 23–59.

Dalla Torre, M., Stern, W. B. & Frey, M. (1994). Determination of white K-mica polytype ratios: comparison of different XRD methods. *Clay Minerals* **29**, 717–726.

Dalla Torre, M., de Capitani, C., Frey, M., Underwood, M. B., Mullis, J. & Cox, C. (1996*a*). Very-low temperature metamorphism of shales from the Diablo Range, Franciscan complex, California: new constraints on the exhumation path. *Geological Society of America Bulletin* **108**, 578–601.

Dalla Torre, M., Livi, K. J. T. & Frey, M. (1996*b*). Chlorites textures and composition from high pressure/low temperature metashales and metagraywackes, Franciscan complex, Diablo Range, California, U.S.A. *European Journal of Mineralogy* **8**, 825–846.

Dalla Torre, M., Ferreiro Mählmann, R. & Ernst, W. G. (1997). Experimental study on the pressure dependence of vitrinite maturation. *Geochimica et Cosmochimica Acta* **61**, 2921–2928.

de Capitani, C. (1994). *Gleichgewichts-Phasendiagramme: Theorie und Software. Berichte der Deutschen Mineralogischen Gesellschaft, Beihefte zum European Journal of Mineralogy* **6**, 1–48.

de Capitani, C. & Brown, T. H. (1987). The computation of chemical equilibrium in complex systems containing non-ideal solutions. *Geochimica et Cosmochimica Acta* **51**, 2639–2652.

Diessel, C. F. K., Brothers, R. N. & Black, P. M. (1978). Coalification and graphitization in high-pressure schists in New Caledonia. *Contributions to Mineralogy and Petrology* **68**, 63–78.

El-Shazly, A. K. & Liou, J. G. (1991). Glaucophane chloritoid-bearing assemblages from NE Oman: petrologic significance and a petrogenetic grid for high *P* metapelites. *Contributions to Mineralogy and Petrology* **107**, 180–201.

Ernst, W. G. (1963). Significance of phengitic micas from low grade schists. *American Mineralogist* **48**, 1357–1373.

Ernst, W. G. & Banno, S. (1991). Neoblastic jadeitic pyroxene in Franciscan metagreywackes from Pacheo Pass, central Diablo Range, California, and implications for the inferred metamorphic *P–T* trajectory. *New Zealand Journal of Geology and Geophysics* **34**, 285–292.

Ernst, W. G. & Ferreiro Mählmann, R. (2004). Vitrinite alteration rate as a function of temperature, time, starting material, aqueous fluid pressure and oxygen fugacity—laboratory corroboration of prior work. In: Hill, R. J., Leventhal, J., Aizenshtat, Z., Baedecker, M. J., Claypool, G., Eganhouse, R., Goldhaber, M. & Peters, K. (eds) *Geochemical Investigations in Earth Space Science: a Tribute to Isaac R. Kaplan. Geological Society, Publication* **9**, 341–357.

Fang, H. & Jianyu, C. (1992). The effect of oxidation–reduction conditions on the hydrocarbon potential and thermostability of organic matter. *Earth Sciences* **17**, 45–54.

Feldhoff, R. A., Luecke, A. & Richter, D. K. (1991). Ueber die Diagenese-/Metamorphosebedingungen der Pindos- und Tripolitza-Serie auf der Insel Kreta (Griechenland). *Sediment '90; 5. Treffen Deutschsprachiger Sedimentologen. Zentralblatt für Geologie und Palaeontologie, Teil I: Allgemeine, Angewandte, Regionale und Historische Geologie* **11**, 1611–1622.

Ferreiro Mählmann, R. (1994). Zur Bestimmung von Diagenesehöhe und beginnender Metamorphose-Temperaturgeschichte und Tektogenese des Austroalpins und Süpenninikums in Vorarlberg und Mittelbünden. *Universität Frankfurt, Frankfurter Geowissenschaftliche Arbeiten, Serie C* **14**, 498 pp.

Ferreiro Mählmann, R. (1995). The pattern of diagenesis and metamorphism by vitrinite reflectance and illite-'crystallinity' in Mittelbünden and in the Oberhalbstein. Part 1: The relationship to stockwerk tectonics. *Schweizerische Mineralogische und Petrographische Mitteilungen* **75**, 85–122.

Ferreiro Mählmann, R. (1996). The pattern of diagenesis and metamorphism by vitrinite reflectance and illite-'crystallinity' in Mittelbünden and in the Oberhalbstein. Part 2: Correlation of coal petrographical and of mineralogical parameters. *Schweizerische Mineralogische und Petrographische Mitteilungen* **76**, 23–46.

Ferreiro Mählmann, R. (2001). Correlation of very low grade data to calibrate a thermal maturity model in a nappe tectonic setting, a case study from the Alps. *Tectonophysics* **334**, 1–33.

Ferreiro Mählmann, R., Petrova, T. V., Pironon, J., Stern, W. B., Ghanbaja, J., Dubessy, J. & Frey, M. (2002). Transmission electron microscopy study of carbonaceous material in a metamorphic profile from diagenesis to amphibolite facies (Bünderschiefer, Eastern Switzerland). *Schweizerische Mineralogische und Petrographische Mitteilungen* **82**, 253–272.

Fitzherbert, J. A., Clarke, G. L. & Powell, R. (2003). Lawsonite–omphacite-bearing metabasites of the Pam Peninsula, NE New Caledonia: evidence for disrupted blueschist- to eclogite-facies conditions. *Journal of Petrology* **44**, 1805–1831.

Frey, M., Teichmüller, M., Teichmüller, R., Mullis, J., Künzi, B., Breitschmid, A., *et al.* (1980). Very low-grade metamorphism in external parts of the Central Alps: illite crystallinity, coal rank and fluid inclusion data. *Eclogae Geologicae Helvetiae* **73**, 173–203.

Ghent, E. D., Stout, M., Black, P. M. & Brothers, R. N. (1987). Chloritoid-bearing rocks associated with blueschists and eclogites, northern New Caledonia. *Journal of Metamorphic Geology* **5**, 239–254.

Ghent, E. D., Roddick, J. C. & Black, P. M. (1994). [40]Ar/[39]Ar dating of white micas from the epidote to the omphacite zones, northern New Caledonia: tectonic implications. *Canadian Journal of Earth Sciences* **31**, 995–1001.

Goffé, B. & Velde, B. (1984). Contrasted metamorphic evolution in thrusted cover units of the Briançonnais zone (Franch Alps): a model

for the conservation of HP–LT metamorphic mineral assemblages. *Earth and Planetary Sciences Letters* **68**, 351–360.

Guggenheim, S., Jr, Bain, D. C., Bergaya, F., Brigatti, M. F., Drits, V. A., Eberl, D. D., *et al.* (2002). Report of the Association Internationale pour l'Etude des Argiles (AIPEA) nomenclature committee for 2001: order, disorder and crystallinity in phyllosilicates and the use of the 'crystallinity index'. *Clays and Clay Minerals* **50**, 406–409.

Guidotti, C. V., Sassi, F. P. & Blencoe, J. G. (1989). Compositional controls on the *a* and *b* cell dimensions of 2M1 muscovites. *European Journal of Mineralogy* **1**, 71–84.

Hedenquist, J. W. (1991). Boiling and dilution in the shallow portion of the Waiotapu geothermal system. *Geochimica et Cosmochimica Acta* **55**, 2753–2766.

Hey, M. H. (1954). A new review of the chlorites. *Mineralogical Magazine* **30**, 277–292.

Hollister, L. S. & Crawford, M. L. (1981). *Short Course in Fluid Inclusions: Applications to Petrology. Mineralogical Association of Canada, Short Course Handbook* **6**.

Kisch, H. J. (1987). Correlation between indicators of very low-grade metamorphism. In: Frey, M. (ed.) *Low Temperature Metamorphism*. Glasgow: Blackie, pp. 227–300.

Kretz, R. (1983). Symbols for rock-forming minerals. *American Mineralogist* **68**, 277–279.

Leake, B. L., Woolley, A. R., Arps, C. E. S., Birch, W. D., Gilbert, M. C., Grice, J. *et al.* (1997). Nomenclature of amphiboles: report of the subcommittee on amphiboles of the International Mineralogical Association, Commission on News Minerals and Mineral Names. *American Mineralogist* **82**, 1019–1037.

Le Bayon, R. (2002). Tectono-metamorphic evolution of the Monte Rosa Nappe and surrounding units (Western Alps): implications for alpine geodynamics and exhumation of metamorphic terranes. Ph.D. thesis, University of Basel, 123 pp.

Massonne, H. J. & Szpurka, Z. (1997). Thermodynamic properties of white micas on the basis of high-pressure experiments in the systems K_2O–MgO–Al_2O_3–SiO_2–H_2O and K_2O–FeO–Al_2O_3–SiO_2–H_2O. *Lithos* **41**, 229–250.

Maurizot, P., Eberlé, J.-M., Habault, C. & Tessarollo, C. (1989). Carte géologique à l'échelle du 1/50'000, feuille Pam–Ouégoa. (Map sheet and explanatory notes). Orléans: Bureau de Recherches Géologiques et Minières, 81 pp.

Merriman, R. J., Roberts, B., Peacor, D. R. & Hirons, S. R. (1995). Strain-related differences in the crystal growth of white mica and chlorite: a TEM and XRD study of the development of metapelitic microfabrics in the Southern Uplands thrust terrane, Scotland. *Journal of Metamorphic Geology* **13**, 559–576.

Moore, D. M. & Reynolds, R. C. (1997). *X-Ray Diffraction and the Identification and Analysis of Clay Minerals*. New York: Oxford University Press, 378 pp.

Mullis, J. (1976). Das Wachstumsmilieu der Quarzkristalle im Val d'Illiez (Wallis, Schweiz). *Schweizerische Mineralogische und Petrographische Mitteilungen* **56**, 219–268.

Mullis, J. (1987). Fluid inclusion studies during very low-grade metamorphism. In: Frey, M. (ed.) *Low Temperature Metamorphism*. Glasgow: Blackie, pp. 162–199.

Mullis, J., Dubessy, J., Poty, B. & O'Neil, J. (1994). Fluid regimes during late stage of a continental collision: physical, chemical, and stable isotope measurements of fluid inclusions in fissure quartz from a geotraverse through the Central Alps, Switzerland. *Geochimica et Cosmochimica Acta* **58**, 2239–2267.

Paris, J. P. (1981). *Géologie de la Nouvelle-Calédonie, un Essai de Synthèse*. Orléans: Bureau de Recherches Géologiques et Minières, 240 pp.

Parra, T., Vidal, O. & Agard, P. (2002). A thermodynamic model for Fe–Mg dioctahedral K white micas using data from phase-equilibrium experiments and natural pelitic assemblages. *Contributions to Mineralogy and Petrology* **143**, 706–732.

Potter, R. W., II, Clynne, M. A. & Brown, D. L. (1978). Freezing point depression of aqueous sodium solutions. *Economic Geology* **73**, 284–285.

Poty, B., Leroy, J. & Jachimowicz, L. (1976). Un nouvel appareil pour la mesure des températures sous le microscope: l'installation de microthermométrie Chaixmeca. *Bulletin de Minéralogie* **99**, 182–186.

Ramírez, E. & Sassi, R. (2001). The baric character of the Patagonian basement as deduced from the muscovite $d_{060,331}$ spacing: a first contribution from Eastern Andean Metamorphic Complex (Andes, Chile). *European Journal of Mineralogy* **13**, 1119–1126.

Rawling, T. J. & Lister, G. S. (1999). Oscillating modes of orogeny in the Southwest Pacific and the tectonic evolution of New Caledonia. In: Ring, U., Brandon, M. T., Lister, G. S. & Willett, S. D. (eds) *Exhumation Processes: Normal Faulting, Ductile Flow and Erosion. Geological Society, London, Special Publications* **154**, 109–127.

Sassi, F. P. (1972). The petrological and geological significance of the b_0 values of potassic white micas in low-grade metamorphic rocks. An application to the Eastern Alps. *Tschermaks Mineralogische und Petrographische Mitteilungen* **18**, 105–113.

Sassi, F. P. (1987). Metamorfismo. In: D'Amico, C., Innocenti, F. & Sassi, F. P. (eds) *Magmatismo e metamorfismo*. Torino: UTET, pp. 277–483.

Sassi, F. P. & Scolari, A. (1974). The b_0 of the potassic white micas as a barometric indicator in low-grade metamorphism of pelitic schists. *Contributions to Mineralogy and Petrology* **45**, 143–152.

Schmidt, D., Schmidt, S. Th., Mullis, J., Ferreiro Mählmann, R. & Frey, M. (1997). Very low grade metamorphism of the Taveyanne formation of western Switzerland. *Contributions to Mineralogy and Petrology* **129**, 385–403.

Shepherd, T., Rankin, A. H. & Alderton, D. H. M. (1985). *A Practical Guide to Fluid Inclusion Studies*. Glasgow: Blackie.

Teichmüller, M. (1987). Organic material and very low-grade metamorphism. In: Frey, M. (ed.) *Low Temperature Metamorphism*. Glasgow: Blackie, pp. 114–161.

Underwood, M. B., Bergfeld, D., Brocculeri, T., Kang, S. M., Laughland, M., Orr, R. *et al.* (1991). Correlation among paleotemperature indicators within orogenic belts: examples from pelitic rocks of the Franciscan complex (California), the Shimanto Belt (Japan), and the Kandik Basin (Alaska). *EOS Transactions, American Geophysical Union* **72**, 549.

Valori, A., Cathelineau, M. & Marignac, Ch. (1992). Early fluid migration in a deep part of the Larderello geothermal field: a fluid inclusion study of the granite sill from well Monteverdi 7. *Journal of Volcanology and Geothermal Research* **51,** 115–131.

Van den Kerkhof, A. M. & Hein, F. H. (2001). Fluid inclusion petrography. *Lithos* **55**, 27–47.

Vidal, O. & Parra, T. (2000). Exhumation paths of high-pressure metapelites obtained from local equilibria for chlorite–phengite assemblages. *Geological Journal* **35**, 139–161.

Warr, L. N. & Rice, A. H. (1994). Interlaboratory standardization and calibration of clay mineral crystallinity and crystallite size data. *Journal of Metamorphic Geology* **12**, 141–152.

Wolf, M. (1978). Inkolhungsuntersuchungen im Hunsrück, Rheinisches Schiefergebirge. *Zeitschrift der Deutschen Geologischen Gesellschaft* **129**, 217–227.

Yokoyama, K., Brothers, R. N. & Black, P. M. (1986). Regional eclogite facies in the high-pressure metamorphic belt of New Caledonia. In: Evans, B. W. & Brown, E. H. (eds) *Blueschists and Eclogites. Geological Society of America, Memoirs* **164**, 407–423.

Zane, A. & Weiss, Z. (1998). A procedure for classifying rock-forming chlorites based on microprobe data. *Rendiconti Lincei Scienze Fisiche e Naturali* **9**, 51–56.

Zhang, Y. G. & Frantz, J. D. (1987). Determination of the homogenization temperatures and densities of supercritical fluids in the system NaCl–KCl–CaCl$_2$–H$_2$O using synthetic fluid inclusions. *Chemical Geology* **64**, 335–350.